



HAL
open science

Geochronology and geochemistry of a Neoproterozoic syn-tectonic granitic pluton in the Gari-Gombo area, East Cameroun: Implications for petrogenesis and tectonic evolution

Joseph Martial Akame, Marc Poujol, Vinciane Debaille, Bernhard Schulz, Nathan Cogné, Lise Carole Okomo Atouba, Sébastien Owona

► To cite this version:

Joseph Martial Akame, Marc Poujol, Vinciane Debaille, Bernhard Schulz, Nathan Cogné, et al.. Geochronology and geochemistry of a Neoproterozoic syn-tectonic granitic pluton in the Gari-Gombo area, East Cameroun: Implications for petrogenesis and tectonic evolution. *Chemie der Erde / Geochemistry*, 2024, 84 (3), pp.126161. 10.1016/j.chemer.2024.126161 . insu-04630100

HAL Id: insu-04630100

<https://insu.hal.science/insu-04630100v1>

Submitted on 26 Nov 2024

HAL is a multi-disciplinary open access archive for the deposit and dissemination of scientific research documents, whether they are published or not. The documents may come from teaching and research institutions in France or abroad, or from public or private research centers.

L'archive ouverte pluridisciplinaire **HAL**, est destinée au dépôt et à la diffusion de documents scientifiques de niveau recherche, publiés ou non, émanant des établissements d'enseignement et de recherche français ou étrangers, des laboratoires publics ou privés.

1 **Geochronology and geochemistry of a Neoproterozoic syn-tectonic granitic pluton in the**
2 **Gari-Gombo area, East Cameroun: Implications for petrogenesis and tectonic evolution**

3 Joseph Martial Akame^{1,2*}, Marc Poujol¹, Vinciane Debaille², Bernhard Schulz³, Nathan
4 Cogné¹, Lise Carole Okomo Atouba⁴, Sébastien Owona^{4,5}

5 ¹Univ. Rennes, CNRS, Géosciences Rennes - UMR 6118, F-35000 Rennes, France

6 ²Laboratoire G-Time, Université libre de Bruxelles, CP 160/02, 50 Avenue F.D. Roosevelt,
7 1050, Brussels, Belgium.

8 ³TU Bergakademie Freiberg, Institute of Mineralogy, Division of Economic Geology and
9 Petrology, Brennhausgasse 14, D-09599 Freiberg/Saxony, Germany

10 ⁴Department of Earth and Environmental Sciences, Higher Teacher's Training College,
11 University of Bertoua, P.O. Box 652, Bertoua, Cameroon

12 ⁵Department of Earth Sciences, Faculty of Science, University of Douala, P.O. Box, 24157,
13 Douala, Cameroon

14 *Correspondence: J. M. Akame (akamejosephmartial@gmail.com; joseph.martial.akame@ulb.be)

16 **Abstract**

17 Granites are widespread in many Precambrian orogenic belts worldwide; therefore, they can
18 provide insights into orogenic processes and associated magmatism. Zircon U-Pb age, monazite
19 Th-U-total Pb age and whole-rock geochemical data for a granite pluton from the Gari-Gombo
20 area in the Adamawa-Yade domain of the Central African Fold Belt (CAFB) in East Cameroon
21 are presented. The granite is composed dominantly of perthitic K-feldspars, quartz, plagioclase
22 and minor biotite with accessory monazite, apatite and zircon. LA-ICP-MS zircon U-Pb dating
23 yielded an age at ca 631– 620 Ma, which is interpreted as age of emplacement that coincides
24 with the onset of D2 Pan-African deformation. Monazite grains in Gari-Gombo granite follow

1
2
3
4
5
6
7
8
9
10
11
12
13
14
15
16
17
18
19
20
21
22
23
24
25
26
27
28
29
30
31
32
33
34
35
36
37
38
39
40
41
42
43
44
45
46
47
48
49
50
51
52
53
54
55
56
57
58
59
60
61
62
63
64
65

strictly the huttonite substitution trend in Th + U vs Si coordinates. Monazites give consistent Neoproterozoic ages of 630 ± 4 Ma and 602 ± 4 Ma. indicate that growth history and crystallization age of monazites also correlate well with the Pan-African plutonism and granulite facies metamorphism (ca 614-600 Ma) in the Gari-Gombo area. The Gari-Gombo pluton samples show high-K calc-alkaline magnesian, slightly peraluminous signature, high SiO_2 (70.16–78.80 wt. %), K_2O (4.39–5.38 wt. %), and Rb (165–248 ppm), and low $\text{P}_2\text{O}_5 \leq 0.01$ wt. % and Sr (146–222 ppm) contents. They have highly-fractionated REE pattern ((La/Yb)_N = 6.17–148.18), moderately Eu negative anomalies (Eu/Eu* = 0.53–0.93) and the obviously Nb and Ti negative anomalies. These geochemical features suggest that the Gari-Gombo pluton is a highly fractionated I-type granite generated by partial melting of older meta-igneous materials at middle to lower crustal levels. The 2.9 and 0.95 Ga inherited zircon grains identified within the studied granites further confirm the existence of ancient crust in this region.

Keywords: Central Africa Fold Belt, Neoproterozoic, Granite, Pan-African orogeny, Geochemistry, monazite-Ce, Zircon and monazite petrochronology

1. Introduction

Granitic rocks are the major exposed components of the continental crust and they play an essential role in its generation, differentiation and evolution (Şengör et al., 1991; Cawood et al., 2013; Wang et al., 2023). Granites are considered to be derived either from the partial melting of crustal or oceanic rocks, or the fractional crystallization of magmas in different tectonic settings (Eby, 1992; Barbarin, 1999; Collins and Richards, 2008; Chappell et al., 2012; Brown, 2013; Hinchey et al., 2023). These two primary petrological processes lead to the generation of various granitic magmas, including I, S, M and A-type granites (Chappell, 1974; Martin, 2006), which are widely distributed in Precambrian orogenic belts making these sites the best natural laboratories for the study of growth and reworking of continental crust, as well

1
2
3
4
5
6
7
8
9
10
11
12
13
14
15
16
17
18
19
20
21
22
23
24
25
26
27
28
29
30
31
32
33
34
35
36
37
38
39
40
41
42
43
44
45
46
47
48
49
50
51
52
53
54
55
56
57
58
59
60
61
62
63
64
65
66
67
68
69
70
71
72
73
74
75
76
77
78
79
80
81
82
83
84
85
86
87
88
89
90
91
92
93
94
95
96
97
98
99
100
101
102
103
104
105
106
107
108
109
110
111
112
113
114
115
116
117
118
119
120
121
122
123
124
125
126
127
128
129
130
131
132
133
134
135
136
137
138
139
140
141
142
143
144
145
146
147
148
149
150
151
152
153
154
155
156
157
158
159
160
161
162
163
164
165
166
167
168
169
170
171
172
173
174
175
176
177
178
179
180
181
182
183
184
185
186
187
188
189
190
191
192
193
194
195
196
197
198
199
200
201
202
203
204
205
206
207
208
209
210
211
212
213
214
215
216
217
218
219
220
221
222
223
224
225
226
227
228
229
230
231
232
233
234
235
236
237
238
239
240
241
242
243
244
245
246
247
248
249
250
251
252
253
254
255
256
257
258
259
260
261
262
263
264
265
266
267
268
269
270
271
272
273
274
275
276
277
278
279
280
281
282
283
284
285
286
287
288
289
290
291
292
293
294
295
296
297
298
299
300
301
302
303
304
305
306
307
308
309
310
311
312
313
314
315
316
317
318
319
320
321
322
323
324
325
326
327
328
329
330
331
332
333
334
335
336
337
338
339
340
341
342
343
344
345
346
347
348
349
350
351
352
353
354
355
356
357
358
359
360
361
362
363
364
365
366
367
368
369
370
371
372
373
374
375
376
377
378
379
380
381
382
383
384
385
386
387
388
389
390
391
392
393
394
395
396
397
398
399
400
401
402
403
404
405
406
407
408
409
410
411
412
413
414
415
416
417
418
419
420
421
422
423
424
425
426
427
428
429
430
431
432
433
434
435
436
437
438
439
440
441
442
443
444
445
446
447
448
449
450
451
452
453
454
455
456
457
458
459
460
461
462
463
464
465
466
467
468
469
470
471
472
473
474
475
476
477
478
479
480
481
482
483
484
485
486
487
488
489
490
491
492
493
494
495
496
497
498
499
500
501
502
503
504
505
506
507
508
509
510
511
512
513
514
515
516
517
518
519
520
521
522
523
524
525
526
527
528
529
530
531
532
533
534
535
536
537
538
539
540
541
542
543
544
545
546
547
548
549
550
551
552
553
554
555
556
557
558
559
560
561
562
563
564
565
566
567
568
569
570
571
572
573
574
575
576
577
578
579
580
581
582
583
584
585
586
587
588
589
590
591
592
593
594
595
596
597
598
599
600
601
602
603
604
605
606
607
608
609
610
611
612
613
614
615
616
617
618
619
620
621
622
623
624
625
626
627
628
629
630
631
632
633
634
635
636
637
638
639
640
641
642
643
644
645
646
647
648
649
650
651
652
653
654
655
656
657
658
659
660
661
662
663
664
665
666
667
668
669
670
671
672
673
674
675
676
677
678
679
680
681
682
683
684
685
686
687
688
689
690
691
692
693
694
695
696
697
698
699
700
701
702
703
704
705
706
707
708
709
710
711
712
713
714
715
716
717
718
719
720
721
722
723
724
725
726
727
728
729
730
731
732
733
734
735
736
737
738
739
740
741
742
743
744
745
746
747
748
749
750
751
752
753
754
755
756
757
758
759
760
761
762
763
764
765
766
767
768
769
770
771
772
773
774
775
776
777
778
779
780
781
782
783
784
785
786
787
788
789
790
791
792
793
794
795
796
797
798
799
800
801
802
803
804
805
806
807
808
809
810
811
812
813
814
815
816
817
818
819
820
821
822
823
824
825
826
827
828
829
830
831
832
833
834
835
836
837
838
839
840
841
842
843
844
845
846
847
848
849
850
851
852
853
854
855
856
857
858
859
860
861
862
863
864
865
866
867
868
869
870
871
872
873
874
875
876
877
878
879
880
881
882
883
884
885
886
887
888
889
890
891
892
893
894
895
896
897
898
899
900
901
902
903
904
905
906
907
908
909
910
911
912
913
914
915
916
917
918
919
920
921
922
923
924
925
926
927
928
929
930
931
932
933
934
935
936
937
938
939
940
941
942
943
944
945
946
947
948
949
950
951
952
953
954
955
956
957
958
959
960
961
962
963
964
965
966
967
968
969
970
971
972
973
974
975
976
977
978
979
980
981
982
983
984
985
986
987
988
989
990
991
992
993
994
995
996
997
998
999
1000

as linkages between magmatism and tectonic processes (Cawood et al., 2009). The I- and S-type granites are mainly crustal-derived and collisional and/or subduction-related (Mo et al., 2008; Niu et al., 2013; Gao et al., 2017), whereas the A-type granites are typically peralkaline and emplaced in within-plate or late- to post-collisional settings (Rogers and Greenberg, 1990; Eby, 1990, 1992; Frost and Frost, 2011). Therefore, deciphering the geochemical and geochronological fingerprints of granites can provide useful information about the mechanisms of magma genesis, orogenic processes, and continental assembly and breakup (Şengör et al., 2018; Wang et al., 2023).

58 The Central African Fold Belt (CAFB), also known as the Oubanguides Orogenic belt, is
59 a large Neoproterozoic mobile domain in Cameroon, which was formed by convergence and
60 continental collision between the West African and the Congo-São Francisco Cratons (e.g.,
61 Castaing et al., 1994; Trompette, 1997). The CAFB is subdivided, from north to south, into
62 three main structural units; namely the Western Cameroon, the Adamawa-Yadé (ADY) and the
63 Yaoundé domains respectively (Fig.1b) (e.g., Toteu et al., 2004, 2022). In the last three decades,
64 geologists have carried out detailed structural, metamorphic, geochemical, and
65 geochronological investigations on the CAFB, and obtained large sets of new data and
66 competing interpretations, providing important information for understanding the build-up and
67 evolution of the CAFB (e.g., Toteu et al., 1994, 2001, 2004; Ngako et al., 2003; Tchameni et
68 al., 2006; Penaye et al., 2006; Ganwa et al., 2008; Djouka-Fonkwé et al., 2008; Li et al., 2017;
69 Betsi et al., 2020; Kamguia Kamani et al., 2021; Owona et al., 2021a; Mvondo et al., 2023).
70 The results of these studies demonstrate that the CAFB experienced multiple magmatic,
71 metamorphic and deformation events (D1–D4 phases) during Neoproterozoic time. Although
72 there is consensus that the initial and paroxysmal phases of the Pan-African orogeny in
73 Cameroon took place at ca. 660–580 Ma, with an early nappe tectonics and a subsequent
74 widespread granitoid magmatism (Nzenti et al., 1988; Toteu et al., 2004, 2022; Penaye et al.,

75 2006; Djouka-Fonkwé et al., 2008; Kwékam et al., 2010; Owona et al., 2012; Betsi et al., 2020;
76 Kamguia Kamani et al., 2021), the timing and duration of its polyphase tectono-metamorphic
77 and magmatic events are still disputed. Toteu et al. (2004) suggested that syn-collisional
78 granitoids in CAFB were emplaced during the D1-D2 deformations phase at ca. 640–610 Ma,
79 whereas recent studies proposed an age interval of ca. 630–600 Ma for D2 phase deformations
80 and the associated syn-collisional granitoids (Tchakounté et al., 2017; Li et al., 2017; Kamguia
81 Kamani et al., 2021; Lemdjou et al., 2022). In the Adamawa-Yadé domain of the CAFB, syn-
82 tectonic granites were dated at 730–650 Ma (Nomo et al., 2017; Ngatcha et al., 2022). Similarly,
83 the granitoids of the Sinassi Batholith in the NW Cameroon domain of CAFB were dated
84 between 686 ± 2 and 644 ± 2 Ma and interpreted as emplaced during the Neoproterozoic
85 subduction stages (Houketchang Bouyo et al., 2016). However, the ages of ca. 700 Ma for D1,
86 ca. 630 Ma for D2, and ca. 580–555 Ma for D3-D4 phase deformations were proposed using
87 LA-ICP-MS U-Pb and ^{40}Ar - ^{39}Ar methods from metamorphic rocks of Yaoundé domain (Betsi
88 et al., 2020; Mvondo et al., 2023). In addition to the ca. 750–650 and 650–600 Ma pre- to syn-
89 collisional granitoids, there are volumes of ca. 560–550 Ma post-collisional alkaline potassic
90 granites cropped out in the CAFB (e.g., Toteu et al., 2022, and reference therein). This indicates
91 crustal reworking throughout the CAFB in response to convergence or divergence of ancient
92 continental blocks, with or without the involvement of mantle material. Here, we present field
93 relationships, new U-Pb zircon data, whole-rock chemical composition and electron probe
94 microanalysis (EPMA) Th-U-Pb monazite for granites of the Gari-Gombo pluton belonging to
95 the ADY, east Cameroon (Fig. 1b). The results have implications on the generation of felsic
96 magmas, its source and orogenic processes during the Neoproterozoic Pan-African orogeny, a
97 geodynamic model in the framework of the evolutionary history of the Central African Fold
98 Belt is proposed.

99 **Fig. 1.**

100 2. Geological setting

1
2
3 101 In the CAFB, Meso- to Neoproterozoic granitoid-gneiss complexes and
4
5 102 metasedimentary rocks are well exposed (Fig. 1) (Nzenti et al., 1988; Penaye et al., 1993; Toteu
6
7
8 103 et al., 2001, 2004; Nkoumbou et al., 2014; Bouyo et al., 2015; Tchakounté et al., 2017; Owona
9
10 104 et al., 2021b). Granitoid-gneiss complexes include the > 700 Ma old calc-alkaline and
11
12
13 105 frequently orthogneissified granitoids; pre- to syntectonic orthogneisses, anatectic granites and
14
15 106 syn-tectonic granitoids (ca 660–600 Ma); syn-to post-tectonic alkaline granites and
16
17 107 microgranites (ca 600–500 Ma) as well as last-stage syenitic and gabbroic intrusions (e.g. Toteu
18
19
20 108 et al., 2022 and reference therein). The occurrence of Archean-Paleoproterozoic detrital zircon
21
22 109 grains within the Neoproterozoic supracrustal formation represents part of the ancient Congo
23
24
25 110 craton crustal segment (Ganwa et al., 2008), and the Eburnean belt of Western Central Africa
26
27 111 (Owona et al., 2021b; Tchakounté et al., 2017). Across the CAFB, metasediments are
28
29
30 112 encountered that mainly consist of Meso- to Neoproterozoic medium- to high-grade schists,
31
32 113 quartzites, paragneisses and conglomerate layers (Yaoundé, Bafia, Lom Poli and Rey Bouba
33
34 114 series), deposited between ca. 1000 and 700 Ma (for Yaoundé series, Toteu et al. 2006; Owona
35
36
37 115 et al. 2021), 700 Ma and 665 Ma for the Lom Poli series, (Toteu et al., 2006), ca 645 and 630
38
39 116 Ma for the Rey Bouba series, Bouyo et al. 2015), and between ca. 613 and 600 Ma the syn-
40
41
42 117 tectonic Lom basin (Soba, 1991; Toteu et al., 2006). Lithostratigraphically, the Yaoundé series
43
44 118 is assigned to the Yaoundé domain (Nzenti et al., 1988; Toteu et al., 2006, 2004), whereas that
45
46
47 119 of the Poli and Rey Bouba is assigned to the Western Cameroon domain (Bouyo et al., 2015;
48
49 120 Ngako et al., 2008; Toteu et al., 2006). Both the Bafia and Lom series are lithostratigraphic
50
51
52 121 entities of the Adamawa-Yadé domain (Soba, 1991; Tchakounté et al., 2017). The granitoid-
53
54 122 gneiss complexes and the metasediments were deformed and metamorphosed during the Pan-
55
56 123 African Orogeny (e.g. Toteu et al., 2022 and reference therein).
57
58
59
60
61
62
63
64
65

124 The Adamawa-Yadé domain (ADY) east of the Tcholliré-Banyo shear zone is
125 characterized by the presence of large remnant of Archean-Paleoproterozoic (>2000 Ma) and
126 ca 1000–700 Ma metasediment and orthogneisses (Ganwa et al., 2008; Tchakounté et al., 2017),
127 and numerous Neoproterozoic granitic intrusions. The metasediments and orthogneisses were
128 deformed and metamorphosed under the amphibolite to granulite-facies conditions between
129 821 and 613 Ma (Ganwa et al., 2008; Tchakounté et al., 2017). The syn- to late tectonic
130 granitoids are K-rich I-type granites that surround and intrude the orthogneisses and the
131 metasediments (Fig. 1b; Kwékam et al., 2010; Saha-Fouotsa et al., 2019; Nomo Negue et al.,
132 2021; Ngatcha et al., 2022; Fossi et al., 2022; Lemdjou et al., 2022). The gneisses are proposed
133 to represent the protoliths for the K-rich granites (Saha-Fouotsa et al., 2019; Fossi et al., 2022;
134 Lemdjou et al., 2022). The plutonism in the ADY was initiated by crustal thickening during
135 continental collision along the NW Congo craton, which led to partial melting of the lower
136 crust, with shear zones acting as magma conduits (Ngako et al., 2003; Njanko et al., 2006;
137 Kankeu et al., 2009; Ngatcha et al., 2022). The post-tectonic granitic rocks of the ADY have an
138 alkaline composition and were emplaced between 560 and 550 Ma ago (Toteu et al., 2006).

139 The Gari-Gombo granitic pluton (03°55'25" N/ 015°06'47.1" E) is located in the eastern
140 segment of the Adamawa-Yadé domain at the frontier between Cameroon and Central African
141 Republic (Fig. 1b). Abundant Neoproterozoic granitoids with notable mafic intrusions crop out
142 in this area, which have intruded Proterozoic metamorphic rocks, and are crosscut by late
143 Neoproterozoic post-tectonic granites (Gazel and Gerard, 1954; Gentry et al., 2021; Ngatcha et
144 al., 2019, 2022; Lemdjou et al., 2022). The Neoproterozoic granitoids have been dated between
145 727 and 638 Ma, indicating that they were formed during the pre- to syncollisional stage of the
146 Pan-African orogenesis (Ngatcha et al., 2022; Lemdjou et al., 2022).

147 3. Field observations and petrography

148 The Gari-Gombo granitic pluton is relatively undeformed in its core, whereas its
1 margins are deformed as indicated by the occurrence of flat-laying magmatic foliation marked
2 149 by the alignment of biotite and K-feldspar crystals. The late-stage felsic dykes are common and
3
4 150 appear undeformed in terms of their geometry (Fig. 2a). The granitic rocks are light grey to
5
6 151 reddish medium-to-coarse grained biotite granites commonly associated with centimetre-size
7
8 152 phenocrysts of alkali feldspar. They contain quartz, alkali feldspars (perthitic microcline),
9
10 153 plagioclase, biotite, hornblende, and a variable amount of zircon, monazite, apatite, chlorite,
11
12 154 opaque as accessory minerals (Fig. 2). Quartz occurs as large xenomorphic grains and
13
14 155 commonly exhibits deformation microstructures such as undulous extinction, internal
15
16 156 microfracture and grain boundary migration recrystallisation (Fig. 2). Occasionally, quartz
17
18 157 ribbons are formed and ondulose extinction is observed in plagioclase and alkali feldspar due
19
20 158 to strong deformation. Myrmekite, perthitic and micro-perthitic K-feldspars are common and
21
22 159 plagioclases are partially altered to sericite whereas biotite is partially altered to chlorite.
23
24 160

161 **Fig. 2**

162 **4. Analytical methods**

163 *4.1. Whole-rock geochemical analyses*

164 Four fresh granite samples devoid of secondary alteration were crushed and pulverized
165 using an agate mill and measured for their major oxides and trace elements concentrations at
166 the Laboratoire G-Time at the Université libre de Bruxelles (ULB), Belgium. About 50 mg of
167 each sample was mixed with a stream of high-purity lithium metaborate in a graphite crucible
168 and heated for 10 minutes at 1000 °C. The bead, after cooling, was dissolved for several hours
169 with a stirring magnet in 5% HNO₃. The diluted samples were then measured along with the
170 USGS BHVO-2 and the RGM2 standards to evaluate the accuracy, which is better than 2%
171 (RSD) for each element. Loss on ignition was determined after 1 h at 1000 °C. Trace elements

172 were measured on the Agilent 7700 ICP-MS at ULB, also using USGS BHVO-2 and RGM-2
173 standards. The total reproducibility estimated using multiple USGS rock standards is better than
174 10% (2SD).

175 **4.2. Zircon U–Pb dating**

176 Two biotite granitic samples (GB1 and GB4) were selected for laser ablation–inductively
177 coupled plasma–mass spectrometry (LA-ICP-MS) zircon U-Pb dating. The zircon grains were
178 separated from the crushed samples using the standard heavy-liquid and magnetic separation
179 procedures at Laboratoire G-Time at ULB. Zircon grains were then handpicked under a
180 binocular microscope, and they were casted in epoxy resin and polished for
181 cathodoluminescence (CL) imaging and U-Pb zircon dating analyses using the facilities
182 available at the GeOHeLiS platform (University of Rennes, France). Cathodoluminescence
183 (CL) imaging was carried out on a Reliotron CL system equipped with a digital colour camera.

184 U-Th-Pb isotope measurements on zircon were carried out using an ESI NWR193UC
185 Excimer laser (193 nm wavelength), coupled to a quadripole Agilent 7700x ICP–MS equipped
186 with a dual pumping system to enhance sensitivity (Paquette et al., 2014). Data were corrected
187 for U-Th-Pb fractionation and mass bias by standard bracketing with repeated measurements
188 of the GJ1 zircon standard (Jackson et al., 2004). Along with the samples, the zircon standard
189 91-500 (1065 Ma; Wiedenbeck et al., 1995) was measured to monitor precision and accuracy
190 of the reduction scheme and produced a concordia age of $1064.0 \pm 4.8/9.7$ Ma (N= 12, MSWD=
191 0.63; supplementary data Table S1). Here and throughout this article, tables and figures
192 uncertainties are quoted at 2σ with and without systematic uncertainties propagation, as
193 recommended by Horstwood et al. (2016). Data reduction was carried out with the software
194 Iolite v4 (Paton et al., 2010). No common Pb correction was applied owing to the large isobaric
195 interference between ^{204}Pb and ^{204}Hg . Concordia diagrams and weighted average diagrams have
196 been generated using IsoplotR (Vermeesch, 2018).

197 4.3. Electron probe microanalysis (EPMA) monazite dating

1
2 198 In a first step, thin sections of granite samples were checked for monazite by Scanning
3
4
5 199 Electron Microscope Automated Mineralogy (SEM-AM) methods, as provided by a FEI
6
7 200 Quanta 600F instrument equipped by a MLA 2.9 and 3.1 software platforms (Schulz et al. 2020)
8
9
10 201 at the Geometallurgy Laboratory of TU Bergakademie Freiberg/Saxony, Germany. The SPL
11
12 202 (Selected Phase Lineup) routine combines a backscattered electron (BSE) grey colour value
13
14 203 trigger and single spot EDX-ray spectral analysis. This enables the detection of rare phases,
15
16
17 204 such as monazite, xenotime and zircon, and their surrounding minerals. One receives a
18
19 205 catalogue of images which document grain sizes and shapes, and the microstructural
20
21
22 206 relationships of all monazite, xenotime, and zircon grains within a distance of ~100 µm from
23
24 207 the margin of the target phase. This was used to select specific monazite grains for detailed
25
26
27 208 study by electron probe microanalysis (EPMA) in thin sections. The SPL routine further allows
28
29 209 for grain counts, phase area estimates and monazite mineral associations from the BSE image
30
31 210 analysis.

32
33
34
35 211 For the second step, the sample GB4 was selected for monazite Th–U–Pb dating using
36
37 212 JEOL JXA-8230 electron probe microanalyser at the Institute of Material Science, TU
38
39
40 213 Bergakademie Freiberg/Saxony Germany. Electron probe Th-U-Pb dating is based on the
41
42 214 observation that common Pb in monazite (light rare earth elements (LREEs), Y, Th, Si, Ca)
43
44 215 PO₄ is negligible when compared to radiogenic Pb resulting from the decay of Th and U
45
46
47 216 (Parrish, 1990; Montel et al., 1996). Also, in monazite the diffusion rates for the radiogenic Pb
48
49 217 at high temperatures are extremely low. Cherniak et al. (2004) reported that a 10-mm sized
50
51
52 218 monazite grain would have a Pb closure temperature in excess of 900 °C, given a cooling rate
53
54 219 of 10 °C/Ma. As such, Pb is fixed in the monazite structure, which explains the low tendency
55
56
57 220 of this element to escape from monazite. Also it is generally agreed that radiation damage in
58
59 221 monazite self-anneals over geological periods of time even at relatively low temperatures, thus

222 preventing the accumulation of significant amounts of damage (e.g. Meldrum et al., 1998;
1
2 223 Nasdala et al., 2018).

3
4
5 224 Electron probe microanalysis of the bulk Th, U and Pb concentrations in monazite, at a
6
7
8 225 constant $^{238}\text{U}/^{235}\text{U}$, allows for the calculation of an isochron age (Suzuki and Kato, 2008),
9
10 226 and/or for single domain ages with a considerable error (Montel et al., 1996; Williams et al.,
11
12 227 2017). The analytical conditions comprised 20 kV accelerating voltage, 100 nA probe current,
13
14
15 228 and 5 μm beam diameter. The Ma1 lines of Pb and Th and the Mb1 lines for U of a PETL
16
17 229 crystal in a spectrometer with a capsuled Xe proportional counter were selected for monazite
18
19
20 230 analysis. Calibration of PbMa1 was carried out on a natural crocoite. The ThMa1 was calibrated
21
22 231 on a Madmon reference monazite from a pegmatite with about 11 wt. % ThO_2 (Schulz and
23
24
25 232 Schüssler, 2013). The UMb1 was calibrated on metal reference material. For calibration of REE
26
27 233 the orthophosphates provided by the Smithsonian Institution (Jarosewich and Boatner, 1991)
28
29
30 234 were used. Monazite dating includes measurement of 10–20 age reference monazite Madmon
31
32 235 and application of interference corrections of an YLg line on PbMa and a ThMz-line on UMb.
33
34
35 236 More details of the analytical protocols are reported in Schulz et al. (2019) and Schulz (2021a).
36
37 237 Analyses with measurable contents of Al were omitted from the dataset as well as analyses with
38
39
40 238 totals outside the range from 98.0 to 101.5 wt. %. For calculation of Th-U-Pb ages for single
41
42 239 monazite analyses (Montel et al., 1996) we applied an error in Pb element % of 0.004 to all
43
44
45 240 analyses, which propagates for the reference monazite Madmon with ~ 506 Ma typically to ± 16
46
47 241 Ma (2σ). Monazite ages were further determined using the ThO_2^* –PbO isochrone method
48
49 242 (CHIME) of Suzuki et al. (1994) where ThO_2^* is the sum of the measured ThO_2 plus ThO_2
50
51
52 243 equivalent to the measured UO_2 . This age is based on the slope of a regression line in ThO_2^* vs
53
54 244 PbO coordinates forced through zero. As the calculation of the regression line provides
55
56
57 245 underestimation of the error, in a further step the weighted average ages for monazite
58
59 246 populations were calculated from the single analyses defining the regression line using Isoplot
60
61
62
63
64
65

247 3.0 (Ludwig, 2003). Weighted average ages were also calculated from the ages of single
1
2 248 analyses when a large monazite allowed several analyses, and from clusters composed of small
3
4 249 monazites. As the sizes of most monazite grains are below 50 μm , it was intended to perform a
5
6
7 250 narrow grid of full quantitative analyses. In all analysed samples, the isochron ages and the
8
9
10 251 weighted average ages coincide within the error. The age data are interpreted as the time of
11
12 252 closure for the Th-U-Pb system of monazite during igneous crystallisation and growth, and
13
14 253 recrystallization in the course of an overprint by metamorphism.
15
16

17 254 5. Results

18 255 5.1. LA-ICP-MS U-Pb zircon dating

22 256 LA-ICP-MS U-Pb analytical data for zircons from the two granitic samples are reported
23
24
25 257 in Table 1. Sample GB1 is a leucocratic and fine-to medium-grained biotite granite (Fig. 2c).
26
27 258 Forty-two single spots in situ analyses were conducted on a total of 21 different zircon grains.
28
29
30 259 The analysed grains are generally prismatic to subhedral and 60–200 μm in size. The CL images
31
32 260 reveal that most display core–rim structure and magmatic oscillatory zoning (Fig. 3a). Although
33
34
35 261 the oscillatory zoning is blurred in most grains, probably due to higher U (247–6663 ppm) and
36
37 262 Th (37–1159 ppm) contents (with Th/U: 0.02–0.89, Table 1). There is no correlation between
38
39
40 263 the U/Th ratios and the corresponding apparent dates. Only six zircons are concordant and yield
41
42 264 a concordia date of $623.2 \pm 8.1/9.9$ Ma (MSWD = 0.86, $n = 6$; Fig. 3c). However, a large number
43
44 265 of discordant grain can be used to calculate a weighted mean $^{206}\text{Pb}/^{238}\text{U}$ date of $624.3 \pm 4.1/7.0$
45
46
47 266 Ma (MSWD = 0.44, $n = 31$; Fig. 3d), comparable within uncertainty with the concordia date.
48
49 267 The remaining data are highly discordant and their position are interpreted as a variable addition
50
51
52 268 of common Pb (as demonstrated by very high Pb206c% in Table1).
53

54 269 Table 1

56 270 A medium- to coarse-grained biotite granite sample GB4 was collected from the Lycée of
57
58
59 271 Gari-Gombo (Fig. 1). Zircon grains from this sample are short to elongate prisms with euhedral
60
61
62
63
64
65

272 terminal and vary length 50 μm to 200 μm (Fig. 3b). Most have zircons core-rim structures and
273 display distinct oscillatory zoning with low luminescence in CL images, except some zircons
274 containing inherited cores (Fig. 3b). Most of the rims are too narrow to be analysed. Forty-two
275 spot analyses were conducted on the 27 different zircon grains from sample GB4 (Table 1).
276 These analyses have moderate to high content in U (161–5613 ppm) and Th (11–459 ppm),
277 with Th/U ratios < 0.7 . Nine concordant analyses yield a Concordia date of $630.3 \pm 4.1/7.1$ Ma
278 (MSWD = 0.68, $n = 9$; Fig. 3f). Three other near concordant analyses yield an older date at
279 $942.7 \pm 9.8/12.5$ Ma (MSWD = 1.2, $n = 3$; Fig. 3e) which together with three other analyses,
280 yield a Discordia with an upper intercept date of $2936 \pm 45/47$ Ma (MSWD = 0.68, $n = 6$; Fig.
281 3e). The remaining other analyses are discordant, probably due to variable degree of Pb*
282 (radiogenic Pb) mobilization and the presence of inherited cores (Table 1).

283 **Fig. 3.**

284 *5.2. Monazite composition and chemical Th–U–total Pb dating*

285 The analysed monazite grains in sample GB4 vary in size from 10 up to 200 μm and occur
286 as inclusion in biotite, plagioclase, and K-feldspar, and as discrete grains in the matrix (Fig.4).
287 They can also be found on the boundaries between minerals, such as zircon, biotite and in some
288 cases with coronas of apatite and allanite. Partial decomposition of monazite to apatite are also
289 observed. Monazite chemistry and EPMA Th-U-Pb monazite age are in the Gari-Gombo granite
290 are reported in Table 2.

291 A total of 64 analyses from nine distinct monazite grains were obtained in this sample. In
292 some cases, the larger monazite grains display areas with oscillatory and sector zoning as
293 typical for igneous crystallisation (Schulz, 2021b). Such grains display weighted average ages
294 at around 620 Ma (Fig. 4a, b). Other monazite grains display Th-rich zones (bright in the back-
295 scattered electron (BSE) image) with dates at 620-640 Ma (Fig. 4c, d). Large domains in such
296 grains are gray in BSE image and display dates at < 610 Ma. These parts are interpreted as

297 alteration domains, as they cut across the initial oscillatory and sector zonations. All the
298 monazites can be classified as monazite-Ce. Most monazite follow strictly the huttonite
299 substitution trend in Th + U vs Si. When dates > 605 Ma from unaltered zones are plotted with
300 dates < 605 Ma from the altered zones they follow a trend of decreasing ThO₂ with decreasing
301 ages (Fig. 4e). There is also a tendency toward lower Th + U when monazite analyses < 605
302 Ma from the altered zones are compared to the > 605 Ma monazite analyses from the unaltered
303 domains (Fig. 4f). From all monazite analyses, two sets of ThO₂*-PbO isochrons and weighted
304 mean dates for this sample have been calculated at 630 ± 4 Ma (n=17; MSWD = 0.66) and 602
305 ± 3 Ma (n = 41; MSWD = 1.5).

306 **Fig. 5**

307 **Table 2**

308 **5.3. Major oxides and trace elements composition**

309 To avoid the effects of post-magmatic alteration and weathering, fresh samples were
310 collected from zones lacking obvious weathering and post-magmatic process (Fig. 2). All
311 analysed samples have low loss-on-ignition values (<0.5 wt%) and weak Ce anomalies (Ce/Ce*
312 = 0.29–1.04 average ~ 0.8), indicating limited alteration and weathering (Polat and Hofmann,
313 2003). They have SiO₂ contents ranging from 70.2 to 78.8 wt.% and high K₂O contents (K₂O
314 = 4.39–5.38 wt. %) with low Na₂O/K₂O (Na₂O/K₂O = 0.62–0.77), belong to the high-K, calc-
315 alkaline series (Table 3, Fig. 6a-b). They have low MgO (0.16–0.56 wt.%, Mg# = 32–44) and
316 Al₂O₃ (13–14 wt.%) contents. The Gari-Gombo granites are mainly magnesian and
317 peraluminous (A/CNK = 1.02–1.17), as well as Ni- and Cr-poor (Ni = 0.29–2.09 ppm, Cr
318 undetected) (Fig. 6c-d). They are also characterised by low Sr/Y (3–29).

319 These granites are characterised by strongly fractionated chondrite-normalised REE
320 patterns (La/Yb_{CN} = 6.02–148.65) and display moderate to negative Eu anomalies (Eu/Eu* =
321 0.53– 0.93) (CN: chondrite normalised value of Anders and Grevesse 1989, Fig. 7a). The

322 primitive normalised multi-element patterns are characterized by elevated Rb, Th and U,
323 negative Nb anomalies ($Nb/Nb^* = 0.02-0.15$), positive Pb anomalies ($Pb/Pb^* = 8.1-55.7$),
324 negative to positive Sr anomalies ($Sr/Sr^* = 0.11-0.7$), and negative P-Ti anomalies (Fig. 7b;
325 Primitive mantle normalised values of Sun and McDonough 1989). Sample GB4 shows a
326 relative enrichment in heavy rare earth elements (HREEs) and Y compared to the other three
327 samples. This is due to the occurrence of HREE-Y enriched minerals, such as monazite, in this
328 rock (Fig. 4).

329 Fig. 6

330 **6. Discussion**

331 *6.1. Significance of the new geochronological data*

332 In this study, zircon crystals from two samples of the Gari-Gombo granite pluton (GB1
333 and GB4) show core-rim structure. They show oscillatory zoning or weak zoning, and variable
334 Th/U ratios, indicating that they might have been affected by variable degree of Pb loss during
335 later fluid-induced and/or thermal activity (Wu and Zheng, 2004). Most of the dated grains in
336 GB1 and GB4 are discordant. Nonetheless, we obtained Concordia dates for both samples at
337 $623.2 \pm 8.1/9.9$ Ma and $630.3 \pm 4.1/7.1$ Ma for GB1 and GB4, respectively. These dates are
338 consistent with each other within uncertainty and we interpret them as the emplacement age of
339 the pluton. On GB4, older dates are observed as well, an upper Discordia intercept ca 2940 Ma
340 and a Concordia date ca 940 Ma. We interpreted these as a Mesoarchean inheritance (Ganwa
341 et al., 2008; Tchakounté et al., 2017), with a possible Tonian thermal event. Sample GB4 was
342 later re-analysed by EMPA Th-U-Pb monazite dating and the results show two weighted mean
343 dates of 630 ± 4 Ma and 602 ± 4 Ma. The oldest is coherent with the zircon U-Pb age and is
344 interpreted as the time of crystallization of the original magmatic monazite. The youngest date
345 of 602 ± 4 Ma is interpreted as the time of recrystallization. Partial dissolution-reprecipitation
346 of monazite induced by the presence of various fluids has been shown in experiments and

347 natural examples by Hetherington et al. (2010), Williams et al., (2011), Harlov et al. (2011),
348 Budzyń et al. (2017). This process can be observed in sample GB4 by the alteration of monazite
349 to apatite and allanite. Furthermore, monazite BSE images show that microstructure alteration
350 zones cutting across oscillatory and sector zonation domains yield ages < 605 Ma. This supports
351 an interpretation of a fluid-induced tectono-thermal overprint of igneous monazite. Previous
352 LA-ICP-MS zircon U–Pb dating for granitoids from the Adamawa-Yadé domain yielded ages
353 from 619 to 727 Ma (Asaah et al., 2015; Lemdjou et al., 2022; Ngatcha et al., 2022; Njiekak et
354 al., 2008; Nomo et al., 2017; Tchakounté et al., 2017). The ages of 641–620 Ma are similar to
355 our results within error, while the ages of 727–652 Ma are slightly older, indicating that the
356 syn-tectonic plutonism in the ADY might have been started at ~ 727 Ma. Nevertheless, it is
357 recognized that several Neoproterozoic pluton intrusions in the Adamawa-Yadé domain were
358 emplaced during widespread 660–580 Ma syn-collisional to late-tectonic magmatism (e.g.,
359 Asaah et al., 2015; Azeuda Ndonfack et al., 2022; Caxito et al., 2020; Ngako et al., 2008;
360 Ngatcha et al., 2022; Tchakounté et al., 2017; Toteu et al., 2022, 2004). Our EPMA Th-U-Pb
361 monazite age of ca. 602 Ma corresponds to the regional D2 syn-collisional tectonothermal event
362 (ca 620–580 Ma) that is recorded by zircon, monazite and titanite thermochronology in the
363 Central African Orogenic Belt (Betsi et al., 2020; Bouyo Houketchang et al., 2009; Li et al.,
364 2017; Mvondo et al., 2023; Ngnotue et al., 2012; Owona et al., 2011; Penaye et al., 1993;
365 Tchakounté et al., 2017; Yonta-Ngoune et al., 2010), and could therefore have induced
366 incomplete lead loss in the zircons.

367 Table 3.

368 ***6.2. Petrogenetic origin of Gari-gombo granites***

369 The granite samples of Gari-Gombo pluton display similar geochemical signatures to the
370 biotite and two-micas granitoids (Fig. 6e; Laurent et al., 2014). On a Ce (ppm) vs SiO₂ (wt%)
371 diagram used for discriminating granite types (Fig. 6f; Whalen et al., 1987), most samples

372 except GB1 plot on the field of I-type granite, but the same samples display typical fractionated
1
2 373 granite geochemical characteristic in Fig. 8a. The biotite and two-mica granites are primarily
3
4 374 derived from the partial melting of older igneous rocks with sedimentary inputs (Laurent et al.,
5
6 375 2014). The studied samples are magnesian and weakly peraluminous ($A/CNK = 1.02-1.17$,
7
8
9 376 average ≈ 1.1), and display high-K calc-alkaline affinity, low Fe_2O_3 , TiO_2 , MgO , Cr and Ni
10
11 377 contents and $Mg\#$ values (Table 3), indicating a crustal origin. The Rb/Sr ratios show significant
12
13 378 correlation with Rb (Fig. 8b), suggesting that partial melting is the main petrogenetic process
14
15 379 controlling the formation of these granites (e.g., Sun et al., 2021). In the $Al_2O_3/(FeOt + MgO)$
16
17 380 $- 3 \times CaO - 5 \times (K_2O/Na_2O)$ source discriminating diagram, almost all the granites samples plot
18
19 381 into the field of melts derived from tonalitic rocks (Fig. 8c; Laurent et al., 2014). This further
20
21 382 confirms that the older meta-igneous rocks may be the most appropriate source for these crustal-
22
23 383 derived granitic melts. Furthermore, the role of sedimentary inputs in their genesis has been
24
25 384 investigated. The Gari-Gombo granites are magnesian and weakly to strongly peraluminous
26
27 385 rocks ($A/CNK = 1.02-1.17$), and have higher Ba and Rb , low Sr contents with low Rb/Ba and
28
29 386 Rb/Sr ratios suggesting derivation from clay-poor sources (Fig. 8d; Sylvester, 1998). These
30
31 387 incompatible elements are likely controlled by crystal fractionation of feldspar, biotite and
32
33 388 clinopyroxene (Fig. 8e-f). Furthermore, the Gari-Gombo granites are characterized by
34
35 389 superchondritic Rb/Sr (0.75–1.65) ratios and weak to negative Sr and Eu anomalies on the
36
37 390 primitive mantle-normalized diagram (Table 1; Fig. 7b), indicating crystal fractionation of
38
39 391 feldspar (e.g. Halliday et al. 1991). The high A/CNK values of some samples may have resulted
40
41 392 from significant fractional crystallization of amphibole (Cawthorn et al., 1976). Negative Nb
42
43 393 and Ti anomalies in the primitive mantle-normalized patterns are controlled by crystallisation
44
45 394 of titanite, whereas enrichment in LREEs on chondritic normalized patterns implies the
46
47 395 crystallisation of monazite or zircon (Fig. 7a-b) (Foley et al., 2000; Rollinson and Pease, 2021).
48
49
50
51
52
53
54
55
56
57
58
59
60
61
62
63
64
65

396 Previous studies suggested that the Neoproterozoic granites in the East region of Cameroon
1
2 397 (like Ngoura, Colomine, Batouri, Fig. 1) were derived from partial melting of a mixed magma
3
4 398 source between crustal-derived melts and a mantle source (Azeuda Ndonfack et al., 2022; Fossi
5
6 399 et al., 2022; Lemdjou et al., 2022; Ngatcha et al., 2022). In the field, there is no geological
7
8 400 evidence that the granites were derived from older mafic rocks, and the lack of elevated Ni, Cr,
9
10 401 Co content and Mg# in the Gari-Gombo granites suggest that the parent magma does not
11
12 402 interact with mantle-derived magma (e.g. Rapp et al. 1999; Smithies 2000). In addition, the
13
14 403 mantle has high Zr/Hf ratio, and low La/Nb, Th/Nb, and Th/La ratios (average value of 37,
15
16 404 0.94, 0.17 and 0.12, respectively; Saunders et al. 1988; Sun and McDonough 1989; Weaver
17
18 405 1991; Pearce 2008), and the addition of mantle materials would enhance those ratios, which is
19
20 406 not the case for the studied Gari-Gombo granites (Zr/Hf = 29–34 average \approx 31, La/Nb = 3–33
21
22 407 average \approx 14, Th/Nb = 1.6–7 average \approx 4 and Th/La = 0.15–0.51 average \approx 0.38 ratios). On the
23
24 408 contrary, these ratios all reflect the characteristics of a crustal source (11.4, 2.20, 0.44, and 0.20,
25
26 409 respectively; Saunders et al. 1988; Weaver 1991; Pearce 2008). On the ternary source
27
28 410 discrimination diagram (Fig. 9a), the biotite granites of Gari-Gombo display heterogeneous
29
30 411 geochemical signatures of melt derived from meta-igneous and metasedimentary rocks (Moyen
31
32 412 et al., 2017). This observation suggest that the Gari-Gombo granites had possibly evolved from
33
34 413 the melting of a heterogeneous source, formed by variable mixing of meta- felsic igneous and
35
36 414 metasedimentary sources. According to the granite classification of Barbarin (1999), the
37
38 415 accessory mineral monazite is characteristic of peraluminous (S-type) granitoids and does not
39
40 416 occur in I-type and metaluminous granitoids. Thus, the observation of monazite in the GB4
41
42 417 granite may signal a poorly homogenized source, with a significant participation of anatectic
43
44 418 melts from metasediments or crustal meta igneous source adding to a mantle source. Most of
45
46 419 samples are characterised by HREE, Sr and Y-depleted (high LREE/HREE (6–44) ratios and
47
48 420 low Sr/Y (3–29) ratio) that reflect retention of garnet in the source. The presence of a \sim 2.9 Ga
49
50
51
52
53
54
55
56
57
58
59
60
61
62
63
64
65

1
2
3
4
5
6
7
8
9
10
11
12
13
14
15
16
17
18
19
20
21
22
23
24
25
26
27
28
29
30
31
32
33
34
35
36
37
38
39
40
41
42
43
44
45
46
47
48
49
50
51
52
53
54
55
56
57
58
59
60
61
62
63
64
65

421 xenocryst zircon in the Gari-Gombo biotite granites suggest that they were derived from
422 reworking of pre-existing Mesoarchean crust. Collectively, we can conclude that the Gari-
423 Gombo granites may be derived from partial melting of ancient meta-igneous materials at
424 middle- to lower crustal levels followed by crystal fractionation. The occurrence of small
425 amounts of inherited zircons (ca. 940 Ma; Fig. 3e; Table 1) may indicate Archean reset zircons
426 as shown by the Discordia (Fig. 3e).

427 **6.3. Tectonic implications**

428 Granitic rocks can be formed in various environments, and their trace element
429 compositions can be used to constrain the tectonic setting responsible for their formation (e.g.
430 Pearce et al. 1984; Eby 1992b). In a Nb-Y-Ce plot (Fig. 9b), the ca. 630 Ma granites in Gari-
431 Gombo area plot mainly in the field of A2-type granites (Eby, 1992), suggesting that their
432 petrogenesis is related to post-collisional extension, as for many highly fractionated granitoids.
433 However, the studied granites show large ion lithophile element (LILE) enrichment (e.g., Rb,
434 Ba, K, U), high field strength element (HFSE) (e.g., Nb and Ti) depletion (Fig. 6e-f), and high
435 Th/Yb>1, suggesting their formation is typical of an arc related setting (Fig. 9e; Thiéblemont
436 and Tegye 1994). However, these chemical features could also be attributed to their crustal
437 source. In a Rb–Nb+Y vs. Nb–Y diagrams (Pearce et al., 1984), most data plot in the syn-
438 collision and volcanic arc granite field (Fig. 9c-d). This suggests that the Gari-Gombo granitic
439 pluton was probably formed in a complex tectonic setting, involving collision and subduction.
440 Numerous Neoproterozoic granitoids formed between 650 and 620 Ma ago in the Adamawa-
441 Yadé domain (Djouka-Fonkwé et al., 2008; Bouyo et al., 2015; Tchakounté et al., 2017;
442 Ngatcha et al., 2019, 2022; Azeuda Ndonfack et al., 2022; Lemdjou et al., 2022; Toteu et al.,
443 2022; Fodoué et al., 2022), at the same time as, or slightly earlier than, ca. 620 Ma D2-
444 deformation and metamorphism, suggesting a close relationship between and tectono-
445 metamorphism and magmatism at that period. This affinity is also evident in the entire Central

446 African Fold Belt (Toteu et al., 2004, 2006, 2022; Djouka-Fonkwé et al., 2008; Tchakounté et
1
2 447 al., 2017; Li et al., 2017; Saha-Fouotsa et al., 2019; Betsi et al., 2020; Owona et al., 2021a;
3
4 448 Mvondo et al., 2023). Although there are different opinions about the cause for the D2 Pan-
5
6
7 449 African tectono-thermal event, most authors considered that the CAFB experienced a
8
9
10 450 collisional tectonic setting during the second stage of the Pan-African orogeny. This inference
11
12 451 is further supported by the distribution of the Gari-Gombo granite samples into the syn-
13
14 452 collisional granite fields in the tectonic discrimination diagram of Batchelor and Bowden (1985)
15
16
17 453 (Fig. 9f). However, a common syn-collisional and magmatic arc character of ca 650–600 Ma
18
19 454 granitoids in the Adamawa-Yadé domain (Asaah et al., 2015; Azeuda Ndonfack et al., 2022;
20
21
22 455 Djouka-Fonkwé et al., 2008; Fodoué et al., 2022; Lemdjou et al., 2022; Ngatcha et al., 2019),
23
24 456 is interpreted as the result of continental collision and subduction between Adamawa-Yadé
25
26
27 457 block and the Congo craton (e.g., Penaye et al., 2006; Lemdjou et al., 2022; Toteu et al., 2022).
28
29 458 Therefore, it is inferred that the Gari-Gombo granite might have been emplaced in a transitional
30
31
32 459 tectonic environment, involving continental collision and subduction.

33 34 460 **7. Conclusions**

35
36
37 461 Granitic rocks of Neoproterozoic age are abundant in the Central African Fold Belt (CAFB)
38
39 462 of Cameroon, recording crustal reworking by multiple episodes of Pan-African intracontinental
40
41
42 463 orogeny. In order to study the Neoproterozoic evolution of this collisional orogen and related
43
44 464 magmatism, we carried out LA-ICP-MS zircon U-Pb dating, EPMA Th-U-Pb monazite data
45
46
47 465 and whole-rock elemental analyses on the Gari-Gombo granitic pluton from Adamawa-Yadé
48
49 466 domain in CAFB, East Cameroon. Our new LA-ICP-MS zircon U-Pb ages combined with
50
51
52 467 EPMA U-Th-Pb monazite data indicate that the granite pluton in the Gari-Gombo pluton was
53
54 468 emplaced between ca. 631–623 Ma, consistent with the D2 Pan-African deformation event,
55
56
57 469 indicating that granitic magmatism and continental collision were coeval. Taking into account
58
59 470 that monazite usually recrystallized during tectono-thermal activity, the U-Th-Pb chemical
60
61
62
63
64
65

1
2
3
4
5
6
7
8
9
10
11
12
13
14
15
16
17
18
19
20
21
22
23
24
25
26
27
28
29
30
31
32
33
34
35
36
37
38
39
40
41
42
43
44
45
46
47
48
49
50
51
52
53
54
55
56
57
58
59
60
61
62
63
64
65

471 monazite age of 602 ± 4 Ma is interpreted as the time of partial dissolution-reprecipitation of
472 igneous monazite during the regional granulite-facies metamorphic event in the Adamawa-
473 Yadé domain. The Gari-Gombo granite shows high-K calc-alkaline, magnesian I-type
474 characteristic with Ba, Nb, Sr, Eu and Ti depletion and distinct positive anomalies in Rb, U, Pb
475 and K. These geochemical features suggest that the of Gari-Gombo granite was formed by
476 partial melting of ancient meta-igneous materials at middle- to lower crustal levels.
477 Subsequently granitic melts have experienced extensive fractional crystallization probably
478 during the magma ascend. The ca. 2.95–0.95 Ga inherited cores in zircon grains provide
479 evidence that the Mesoarchean meta-igneous felsic rocks and Tonian crust were the possible
480 protoliths of the Gari-Gombo granite. These results reinforce evidence of Archean crust
481 previously documented in the Adamawa-Yadé domain.

482 **Acknowledgments**

483 This study was supported by a travel grant “ULB-CCI, Federation Wallonie-Bruxelles”, and
484 the *MOPGA 2022 Visiting Fellowship Program for Young Researchers* from the French
485 Ministries of Europe and Foreign Affairs (MEAE) and of Higher Education, Research and
486 Innovation (MESRI) for current support. JMA thank the FRS-FNRS for Grants and
487 Fellowships" 2023 – Postdocs N° 40017751 and support. VD also thank the FRS-FNRS for
488 support. Numerous rock thin sections were prepared by R. Würkert and M. Stoll at the
489 Helmholtz Institute Freiberg for Resource Technology. Technical support during electron probe
490 microanalyses (INST-FUGG 267/156-1) of monazite at Institute of Materials Science, and
491 SEM-AM sessions at the Geometallurgy Laboratory at TU Bergakademie Freiberg/Saxony
492 were provided by A. Treichel and S. Gilbricht. JMA and VD thank Wendy Debouge for support
493 in geochemical analyses at Laboratoire G-Time. We also appreciate Prof. Astrid Holzheid for
494 his helpful editorial comments and two anonymous reviewers for their detailed and constructive
495 comments that highly improved the paper.

496 References

- 1
2
3 497 Anders, E., Grevesse, N., 1989. Abundances of the elements: Meteoritic and solar. *Geochimica*
4
5 498 *et Cosmochimica Acta* 53, 197–214. [https://doi.org/10.1016/0016-7037\(89\)90286-X](https://doi.org/10.1016/0016-7037(89)90286-X)
6
7
8 499 Asaah, A.V., Zoheir, B., Lehmann, B., Frei, D., Burgess, R., Suh, C.E., 2015. Geochemistry
9
10 500 and geochronology of the 620 Ma gold-associated Batouri granitoids, Cameroon.
11
12 *International Geology Review* 57, 1485–1509.
13 501 <https://doi.org/10.1080/00206814.2014.951003>
14
15 502
16
17 503 Azeuda Ndonfack, K.I., Xie, Y., Zhong, R., Yomeun, B.S., Cui, K., Shan, X., 2022. Tectonic
18
19 evolution of Neoproterozoic rocks, eastern Cameroon: Implication for gold
20 504 mineralization in the Bétaré Oya and Woumbou–Colomine–Kette districts. *Precambrian*
21
22 505 *Research* 368, 106475. <https://doi.org/10.1016/j.precamres.2021.106475>
23
24 506
25
26
27 507 Barbarin, B., 1999. A review of the relationships between granitoid types, their origins and their
28
29 geodynamic environments. *Lithos* 46, 605–626. <https://doi.org/10.1016/S0024->
30 508 [4937\(98\)00085-1](https://doi.org/10.1016/S0024-4937(98)00085-1)
31
32 509
33
34 510 Batchelor, R.A., Bowden, P., 1985. Petrogenetic interpretation of granitoid rock series using
35
36 multicationic parameters. *Chemical Geology* 48, 43–55. <https://doi.org/10.1016/0009->
37 511 [2541\(85\)90034-8](https://doi.org/10.1016/0009-2541(85)90034-8)
38
39 512
40
41
42 513 Betsi, T.B., Ngo Bidjeck Bondje, L.M., Mvondo, H., Yannick Mama Nga, L.N., Molotouala,
43
44 514 C.A., McFarlane, C., 2020. Rutile LA-ICP-MS U–Pb geochronology and implications
45
46 for tectono-metamorphic evolution in the Yaoundé Group of the Neoproterozoic Central
47 515 African Orogeny. *Journal of African Earth Sciences* 171, 103939.
48
49 516 <https://doi.org/10.1016/j.jafrearsci.2020.103939>
50
51 517
52
53
54 518 Bouyo Houketchang, M., Toteu, S.F., Deloule, E., Penaye, J., Van Schmus, W.R., 2009. U–Pb
55
56 519 and Sm–Nd dating of high-pressure granulites from Tcholliré and Banyo regions:
57
58 Evidence for a Pan-African granulite facies metamorphism in north-central Cameroon.
59 520
60
61
62
63
64
65

521 Journal of African Earth Sciences 54, 144–154.
1
2 522 <https://doi.org/10.1016/j.jafrearsci.2009.03.013>
3
4 523 Bouyo, M.H., Zhao, Y., Penaye, J., Zhang, S.H., Njel, U.O., 2015. Neoproterozoic subduction-
5
6
7 524 related metavolcanic and metasedimentary rocks from the Rey Bouba Greenstone Belt
8
9 525 of north-central Cameroon in the Central African Fold Belt: New insights into a
10
11 526 continental arc geodynamic setting. *Precambrian Research* 261, 40–53.
12
13 527 <https://doi.org/10.1016/j.precamres.2015.01.012>
14
15
16 528 Brown, M., 2013. Granite: From genesis to emplacement. Geological Society of America
17
18 529 Bulletin 125, 1079–1113. <https://doi.org/10.1130/B30877.1>
19
20
21 530 Budzyń, B., Harlov, D.E., Kozub-Budzyń, G.A., Majka, J., 2017. Experimental constraints on
22
23 531 the relative stabilities of the two systems monazite-(Ce) – allanite-(Ce) – fluorapatite
24
25 532 and xenotime-(Y) – (Y,HREE)-rich epidote – (Y,HREE)-rich fluorapatite, in high Ca
26
27 533 and Na-Ca environments under P-T conditions of 200–1000 MPa and 450–750 °C.
28
29
30 534 *Miner Petrol* 111, 183–217. <https://doi.org/10.1007/s00710-016-0464-0>
31
32
33 535 Castaing, C., Feybesse, J.L., Thiéblemont, D., Triboulet, C., Chèvremont, P., 1994.
34
35 536 Palaeogeographical reconstructions of the Pan-African/Brasiliano orogen: closure of an
36
37 537 oceanic domain or intracontinental convergence between major blocks? *Precambrian*
38
39 538 *Research* 69, 327–344. [https://doi.org/10.1016/0301-9268\(94\)90095-7](https://doi.org/10.1016/0301-9268(94)90095-7)
40
41
42 539 Cawood, P.A., Kröner, A., Collins, W.J., Kusky, T.M., Mooney, W.D., Windley, B.F., 2009.
43
44 540 Accretionary orogens through Earth history. Geological Society, London, Special
45
46 541 Publications 318, 1–36. <https://doi.org/10.1144/SP318.1>
47
48
49 542 Cawood, P.A., Wang, Y., Xu, Y., Zhao, G., 2013. Locating South China in Rodinia and
50
51 543 Gondwana: A fragment of greater India lithosphere? *Geology* 41, 903–906.
52
53 544 <https://doi.org/10.1130/G34395.1>
54
55
56
57
58
59
60
61
62
63
64
65

- 545 Cawthorn, R.G., Strong, D.F., Brown, P.A., 1976. Origin of corundum-normative intrusive and
1
2 546 extrusive magmas. *Nature* 259, 102–104. <https://doi.org/10.1038/259102a0>
3
- 4 547 Caxito, F. de A., Santos, L.C.M. de L., Ganade, C.E., Bendaoud, A., Fettous, E.-H., Bouyo,
5
6
7 548 M.H., 2020. Toward an integrated model of geological evolution for NE Brazil-NW
8
9 549 Africa: The Borborema Province and its connections to the Trans-Saharan (Benino-
10
11
12 550 Nigerian and Tuareg shields) and Central African orogens. *Braz. J. Geol.* 50.
13
- 14 551 Chappell, B.W., 1999. Aluminium saturation in I- and S-type granites and the characterization
15
16 552 of fractionated haplogranites. *Lithos* 46, 535–551. <https://doi.org/10.1016/S0024->
17
18 553 [4937\(98\)00086-3](https://doi.org/10.1016/S0024-4937(98)00086-3)
19
20
- 21 554 Chappell, B.W., 1974. Two contrasting granite types. *Pacif. Geol.* 8, 173–174.
22
23
- 24 555 Chappell, B.W., Bryant, C.J., Wyborn, D., 2012. Peraluminous I-type granites. *Lithos*, Seventh
25
26 556 Hutton Symposium on Granites and Related Rocks 153, 142–153.
27
28 557 <https://doi.org/10.1016/j.lithos.2012.07.008>
29
30
- 31 558 Chappell, B.W., White, A.J.R., 1992. I- and S-type granites in the Lachlan Fold Belt. *Earth and*
32
33 559 *Environmental Science Transactions of the Royal Society of Edinburgh* 83, 1–26.
34
35 560 <https://doi.org/10.1017/S0263593300007720>
36
37
- 38 561 Chen, A., Zhou, D., Zhang, Q., Yang, Z., 2018. Age, Geochemistry, and Tectonic Implications
39
40 562 of Dulaerqiao Granite, Inner Mongolia. *J. Earth Sci.* 29, 78–92.
41
42 563 <https://doi.org/10.1007/s12583-017-0817-6>
43
44
- 45 564 Cherniak, D.J., Watson, E.B., Grove, M., Harrison, T.M., 2004. Pb diffusion in monazite: a
46
47 565 combined RBS/SIMS study. *Geochimica et Cosmochimica Acta* 68, 829–840.
48
49 566 <https://doi.org/10.1016/j.gca.2003.07.012>
50
51
- 52 567 Collins, W.J., Richards, S.W., 2008. Geodynamic significance of S-type granites in circum-
53
54 568 Pacific orogens. *Geology* 36, 559–562. <https://doi.org/10.1130/G24658A.1>
55
56
57
58
59
60
61
62
63
64
65

- 569 Djouka-Fonkwé, M.L., Schulz, B., Schüssler, U., Tchouankoué, J.-P., Nzolang, C., 2008.
1
2 570 Geochemistry of the Bafoussam Pan-African I- and S-type granitoids in western
3
4 571 Cameroon. *Journal of African Earth Sciences* 50, 148–167.
5
6
7 572 <https://doi.org/10.1016/j.jafrearsci.2007.09.015>
8
- 9
10 573 Drummond, M.S., Defant, M.J., Kepezhinskas, P.K., 1996. Petrogenesis of slab-derived
11
12 574 trondhjemite–tonalite–dacite/adakite magmas. *Earth and Environmental Science*
13
14 575 *Transactions of the Royal Society of Edinburgh* 87, 205–215.
15
16 576 <https://doi.org/10.1017/S0263593300006611>
17
18
- 19 577 Eby, G.N., 1992. Chemical subdivision of the A-type granitoids: Petrogenetic and tectonic
20
21 578 implications. *Geol* 20, 641. [https://doi.org/10.1130/0091-](https://doi.org/10.1130/0091-7613(1992)020<0641:CSOTAT>2.3.CO;2)
22
23 579 [7613\(1992\)020<0641:CSOTAT>2.3.CO;2](https://doi.org/10.1130/0091-7613(1992)020<0641:CSOTAT>2.3.CO;2)
24
25
- 26 580 Eby, G.N., 1990. The A-type granitoids: A review of their occurrence and chemical
27
28 581 characteristics and speculations on their petrogenesis. *Lithos* 26, 115–134.
29
30 582 [https://doi.org/10.1016/0024-4937\(90\)90043-Z](https://doi.org/10.1016/0024-4937(90)90043-Z)
31
32
33
- 34 583 Ewart, A., Griffin, W.L., 1994. Application of proton-microprobe data to trace-element
35
36 584 partitioning in volcanic rocks. *Chemical Geology* 117, 251–284.
37
38 585 [https://doi.org/10.1016/0009-2541\(94\)90131-7](https://doi.org/10.1016/0009-2541(94)90131-7)
39
40
- 41 586 Fodoué, Y., Yannah, M., Tchameni, R., Wassouo, W.J., Kepnamou, A.D., Penaye, J., Mahamat,
42
43 587 A., Negue, E.N., 2022. Peraluminous granitoids within the Hangloa area, Adamawa-
44
45 588 Yadé Domain, Cameroon: Petrogenesis and tectonic implication. *Acta Geochim* 41,
46
47 589 1104–1122. <https://doi.org/10.1007/s11631-022-00565-8>
48
49
50
- 51 590 Foley, S.F., Barth, M.G., Jenner, G.A., 2000. Rutile/melt partition coefficients for trace
52
53 591 elements and an assessment of the influence of rutile on the trace element characteristics
54
55 592 of subduction zone magmas. *Geochimica et Cosmochimica Acta* 64, 933–938.
56
57 593 [https://doi.org/10.1016/S0016-7037\(99\)00355-5](https://doi.org/10.1016/S0016-7037(99)00355-5)
58
59
60
61
62
63
64
65

- 594 Fossi, D.H., Ganno, S., Nzepang Tankwa, M., Soh Tamehe, L., Ayonta Kenné, P., Kouayep
1
2 595 Tchoundi, C.L., Kankeu, B., Nzenti, J.P., 2022. Petrogenesis and tectonic setting of the
3
4 596 Pan-African Deng-Deng intrusive complex in the Lom series, Eastern Cameroon.
5
6
7 597 Journal of African Earth Sciences 188, 104484.
8
9
10 598 <https://doi.org/10.1016/j.jafrearsci.2022.104484>
- 11
12 599 Frost, B.R., Barnes, C.G., Collins, W.J., Arculus, R.J., Ellis, D.J., Frost, C.D., 2001. A
13
14 600 geochemical classification for granitic rocks. *Journal of petrology* 42, 2033–2048.
- 15
16
17 601 Frost, C.D., Frost, B.R., 2011. On Ferroan (A-type) Granitoids: their Compositional Variability
18
19 602 and Modes of Origin. *Journal of Petrology* 52, 39–53.
20
21 603 <https://doi.org/10.1093/petrology/egq070>
- 22
23
24 604 Ganwa, A.A., Frisch, W., Siebel, W., Ekodeck, G.E., Shang, C.K., Ngako, V., 2008. Archean
25
26 605 inheritances in the pyroxene–amphibole-bearing gneiss of the Méiganga area (Central
27
28 606 North Cameroon): Geochemical and 207Pb/206Pb age imprints. *Comptes Rendus*
29
30 607 *Geoscience* 340, 211–222. <https://doi.org/10.1016/j.crte.2007.12.009>
- 31
32
33
34 608 Gao, P., Zheng, Y.-F., Zhao, Z.-F., 2017. Triassic granites in South China: A geochemical
35
36 609 perspective on their characteristics, petrogenesis, and tectonic significance. *Earth-*
37
38 610 *Science Reviews* 173, 266–294. <https://doi.org/10.1016/j.earscrev.2017.07.016>
- 39
40
41 611 Gazel, J., Gerard, G., 1954. Carte géologique de reconnaissance du Cameroun au 1/500000,
42
43 612 feuille de Batouri-Est avec notice explicative. Mémoire Direction des Mines et de la
44
45 613 Géologie, Yaoundé, Cameroun.
- 46
47
48 614 Gentry, F.C., Tchakounte, N.J., Kundu, O.M., Tchop, J.L., Nkoumbou, C., 2021. Four Pan-
49
50 615 African plutonic sets of the Colomines gold district (East-Cameroon): Petrogenesis, K-
51
52 616 Ar dating and geodynamic significance. *Journal of African Earth Sciences* 181, 104220.
53
54 617 <https://doi.org/10.1016/j.jafrearsci.2021.104220>
- 55
56
57
58
59
60
61
62
63
64
65

- 618 Halliday, A.N., Davidson, J.P., Hildreth, W., Holden, P., 1991. Modelling the petrogenesis of
1 high Rb/Sr silicic magmas. *Chemical Geology, Geochemistry of Granitoid Rocks* 92,
2
3 619
4 107–114. [https://doi.org/10.1016/0009-2541\(91\)90051-R](https://doi.org/10.1016/0009-2541(91)90051-R)
5 620
6
- 7 621 Harlov, D.E., Wirth, R., Hetherington, C.J., 2011. Fluid-mediated partial alteration in monazite:
8
9 622 the role of coupled dissolution–reprecipitation in element redistribution and mass
10
11 623 transfer. *Contrib Mineral Petrol* 162, 329–348. [https://doi.org/10.1007/s00410-010-](https://doi.org/10.1007/s00410-010-010-0599-7)
12
13 624
14 0599-7
15
- 16 625 Hetherington, C.J., Harlov, D.E., Budzyń, B., 2010. Experimental metasomatism of monazite
17
18 626 and xenotime: mineral stability, REE mobility and fluid composition. *Miner Petrol* 99,
19
20 627 165–184. <https://doi.org/10.1007/s00710-010-0110-1>
21
22 628
23
- 24 628 Hinchey, A.M., Sandeman, H.A., Butler, J.P., 2023. The Paleoproterozoic granite factory:
25
26 629 Voluminous post-collisional, ferroan, A-type granites and implications for crust
27
28 630 formation and metallogenic tenor, Labrador, Canada. *GSA Bulletin* 136, 893–916.
29
30 631
31 <https://doi.org/10.1130/B36727.1>
32
33
- 34 632 Horstwood, M.S.A., Košler, J., Gehrels, G., Jackson, S.E., McLean, N.M., Paton, C., Pearson,
35
36 633 N.J., Sircombe, K., Sylvester, P., Vermeesch, P., Bowring, J.F., Condon, D.J., Schoene,
37
38 634 B., 2016. Community-Derived Standards for LA - ICP - MS U-(Th-)Pb Geochronology
39
40 635 – Uncertainty Propagation, Age Interpretation and Data Reporting. *Geostandard*
41
42 636 *Geoanalytic Res* 40, 311–332. <https://doi.org/10.1111/j.1751-908X.2016.00379.x>
43
44 637
45
- 46 637 Houketchang Bouyo, M., Penaye, J., Njel, U.O., Moussango, A.P.I., Sep, J.P.N., Nyama, B.A.,
47
48 638 Wassou, W.J., Abaté, J.M.E., Yaya, F., Mahamat, A., Ye, H., Wu, F., 2016.
49
50 639 Geochronological, geochemical and mineralogical constraints of emplacement depth of
51
52 640 TTG suite from the Sinassi Batholith in the Central African Fold Belt (CAFB) of
53
54 641 northern Cameroon: Implications for tectonomagmatic evolution. *Journal of African*
55
56 642 *Earth Sciences* 116, 9–41. <https://doi.org/10.1016/j.jafrearsci.2015.12.005>
57
58
59
60
61
62
63
64
65

- 643 Jackson, S.E., Pearson, N.J., Griffin, W.L., Belousova, E.A., 2004. The application of laser
1
2 644 ablation-inductively coupled plasma-mass spectrometry to in situ U–Pb zircon
3
4 645 geochronology. *Chemical Geology* 211, 47–69.
5
6
7 646 <https://doi.org/10.1016/j.chemgeo.2004.06.017>
8
- 9 647 Jarosewich, E., Boatner, L.A., 1991. Rare-Earth Element Reference Samples for Electron
10
11 648 Microprobe Analysis. *Geostandards and Geoanalytical Research* 15, 397–399.
12
13 649 <https://doi.org/10.1111/j.1751-908X.1991.tb00115.x>
14
15
- 16 650 Ju, Y., Zhang, X., Lai, S., Qin, J., 2017. Permian–Triassic highly-fractionated I-type granites
17
18 651 from the southwestern Qaidam Basin (NW China): Implications for the evolution of the
19
20 652 paleo-tethys in the eastern Kunlun orogenic belt. *J. Earth Sci.* 28, 51–62.
21
22 653 <https://doi.org/10.1007/s12583-017-0745-5>
23
24
- 25 654 Kamguia Kamani, M.S., Wang, W., Tchouankoue, J.-P., Huang, S.-F., Yomeun, B., Xue, E.-
26
27 655 K., Lu, G.-M., 2021. Neoproterozoic syn-collision magmatism in the Nkondjock region
28
29 656 at the northern border of the Congo craton in Cameroon: Geodynamic implications for
30
31 657 the Central African orogenic belt. *Precambrian Research* 353, 106015.
32
33 658 <https://doi.org/10.1016/j.precamres.2020.106015>
34
35
- 36 659 Kankeu, B., Greiling, R.O., Nzenti, J.P., 2009. Pan-African strike–slip tectonics in eastern
37
38 660 Cameroon—Magnetic fabrics (AMS) and structure in the Lom basin and its gneissic
39
40 661 basement. *Precambrian Research* 174, 258–272.
41
42 662 <https://doi.org/10.1016/j.precamres.2009.08.001>
43
44
45
- 46 663 King, P.L., White, A.J.R., Chappell, B.W., Allen, C.M., 1997. Characterization and Origin of
47
48 664 Aluminous A-type Granites from the Lachlan Fold Belt, Southeastern Australia. *Journal*
49
50 665 *of Petrology* 38, 371–391. <https://doi.org/10.1093/petroj/38.3.371>
51
52
53
- 54 666 Kwékam, M., Liégeois, J.-P., Njonfang, E., Affaton, P., Hartmann, G., Tchoua, F., 2010.
55
56 667 Nature, origin and significance of the Fomopéa Pan-African high-K calc-alkaline
57
58
59
60
61
62
63
64
65

668 plutonic complex in the Central African fold belt (Cameroon). *Journal of African Earth*
1
2 669 *Sciences* 57, 79–95. <https://doi.org/10.1016/j.jafrearsci.2009.07.012>
3
4
5 670 Laurent, O., Martin, H., Moyen, J.F., Doucelance, R., 2014. The diversity and evolution of late-
6
7 671 Archean granitoids: Evidence for the onset of “modern-style” plate tectonics between
8
9 672 3.0 and 2.5Ga. *Lithos* 205, 208–235. <https://doi.org/10.1016/j.lithos.2014.06.012>
10
11
12 673 Lemdjou, Y.B., Li, H., Whattam, S.A., Azeuda Ndonfack, K.I., Tchato Tchaptchet, D.P.I.,
13
14 674 Ketchaya, Y.B., Ataquaye Quaye, J., Nguimatsia Dongmo, F.W., 2022. Petrogenesis,
15
16 675 tectonic setting and geodynamic implications of Ouaden, Doumba Bello, and Ngoura
17
18 676 granitic plutons (Eastern Cameroon): Constraints from elemental and Sr–Nd–Hf
19
20 677 isotopic data and zircon U–Pb ages. *Lithos* 418–419, 106682.
21
22 678 <https://doi.org/10.1016/j.lithos.2022.106682>
23
24
25
26 679 Li, X.-H., Chen, Y., Tchouankoue, J.P., Liu, C.-Z., Li, J., Ling, X.-X., Tang, G.-Q., Liu, Y.,
27
28 680 2017. Improving geochronological framework of the Pan-African orogeny in
29
30 681 Cameroon: New SIMS zircon and monazite U-Pb age constraints. *Precambrian*
31
32 682 *Research* 294, 307–321. <https://doi.org/10.1016/j.precamres.2017.04.006>
33
34
35
36 683 Ludwig, K.R., 2009. Isoplot 4.1. A geochronological toolkit for Microsoft Excel.
37
38
39 684 Ludwig, K.R., 2003. User’s manual for IsoPlot 3.0. A geochronological toolkit for Microsoft
40
41 685 Excel 71.
42
43
44 686 Luo, N., Gao, L., Zhang, J., Zhang, Z., Wu, J., Cui, J., Xing, J., 2022. Geochronology and
45
46 687 geochemistry of Early Cretaceous granitic plutons in northern Great Xing’an Range,
47
48 688 NE China, and implications for geodynamic setting. *Open Geosciences* 14, 1206–1237.
49
50
51 689 <https://doi.org/10.1515/geo-2022-0422>
52
53
54 690 Martin, R.F., 2006. A-type granites of crustal origin ultimately result from open-system
55
56 691 fenitization-type reactions in an extensional environment. *Lithos, Peralkaline Rocks* 91,
57
58 692 125–136. <https://doi.org/10.1016/j.lithos.2006.03.012>
59
60
61
62
63
64
65

- 693 Meldrum, A., Boatner, L.A., Weber, W.J., Ewing, R.C., 1998. Radiation damage in zircon and
1
2 694 monazite. *Geochimica et Cosmochimica Acta* 62, 2509–2520.
3
4 695 [https://doi.org/10.1016/S0016-7037\(98\)00174-4](https://doi.org/10.1016/S0016-7037(98)00174-4)
5
6
7 696 Middlemost, E.A.K., 1994. Naming materials in the magma/igneous rock system. *Earth-*
8
9 697 *Science Reviews* 37, 215–224. [https://doi.org/10.1016/0012-8252\(94\)90029-9](https://doi.org/10.1016/0012-8252(94)90029-9)
10
11
12 698 Mo, X., Niu, Y., Dong, G., Zhao, Z., Hou, Z., Zhou, S., Ke, S., 2008. Contribution of
13
14 699 syncollisional felsic magmatism to continental crust growth: A case study of the
15
16 700 Paleogene Linzizong volcanic Succession in southern Tibet. *Chemical Geology* 250,
17
18 701 49–67. <https://doi.org/10.1016/j.chemgeo.2008.02.003>
19
20
21 702 Montel, J.-M., Foret, S., Veschambre, M., Nicollet, C., Provost, A., 1996. Electron microprobe
22
23 703 dating of monazite. *Chemical Geology* 131, 37–53. [https://doi.org/10.1016/0009-](https://doi.org/10.1016/0009-2541(96)00024-1)
24
25 704 [2541\(96\)00024-1](https://doi.org/10.1016/0009-2541(96)00024-1)
26
27
28 705 Moyen, J.-F., 2019. Archean granitoids: classification, petrology, geochemistry and origin.
29
30 706 Geological Society, London, Special Publications SP489-2018–34.
31
32 707 <https://doi.org/10.1144/SP489-2018-34>
33
34
35 708 Moyen, J.-F., Laurent, O., Chelle-Michou, C., Couzinié, S., Vanderhaeghe, O., Zeh, A.,
36
37 709 Villaros, A., Gardien, V., 2017. Collision vs. subduction-related magmatism: Two
38
39 710 contrasting ways of granite formation and implications for crustal growth. *Lithos*,
40
41 711 Eighth Hutton Symposium on Granites and Related Rocks 277, 154–177.
42
43 712 <https://doi.org/10.1016/j.lithos.2016.09.018>
44
45
46
47 713 Mvondo, H., Betsi, T.B., McFarlane, C.R.M., Ondo, J.M., Archibald, D.A., 2023. U-Pb and
48
49 714 Ar-Ar geochronological constraints on timing of deformation and peak metamorphism
50
51 715 in the Central Africa Orogenic Belt, Yaoundé Domain, Cameroon. *International*
52
53 716 *Geology Review* 1–27. <https://doi.org/10.1080/00206814.2023.2225183>
54
55
56
57
58
59
60
61
62
63
64
65

- 717 Nasdala, L., Akhmadaliev, S., Artac, A., Chanmuang N., C., Habler, G., Lenz, C., 2018.
1
2 718 Irradiation effects in monazite–(Ce) and zircon: Raman and photoluminescence study
3
4
5 719 of Au-irradiated FIB foils. *Phys Chem Minerals* 45, 855–871.
6
7 720 <https://doi.org/10.1007/s00269-018-0975-9>
8
- 9
10 721 Ngako, V., Affaton, P., Njonfang, E., 2008. Pan-African tectonics in northwestern Cameroon:
11
12 722 Implication for the history of western Gondwana. *Gondwana Research* 14, 509–522.
13
14 723 <https://doi.org/10.1016/j.gr.2008.02.002>
15
- 16
17 724 Ngako, V., Affaton, P., Nnange, J.M., Njanko, Th., 2003. Pan-African tectonic evolution in
18
19 725 central and southern Cameroon: transpression and transtension during sinistral shear
20
21 726 movements. *Journal of African Earth Sciences* 36, 207–214.
22
23 727 [https://doi.org/10.1016/S0899-5362\(03\)00023-X](https://doi.org/10.1016/S0899-5362(03)00023-X)
24
25
- 26 728 Ngatcha, R.B., Okunlola, O.A., Suh, C.E., Ateh, K.I., Hofmann, A., 2019. Petrochemical
27
28 729 characterization of Neoproterozoic Colomine granitoids, SE Cameroon: Implications
29
30 730 for gold mineralization. *Lithos* 344–345, 175–192.
31
32 731 <https://doi.org/10.1016/j.lithos.2019.06.028>
33
34
- 35
36 732 Ngatcha, R.B., Suh, C.E., Okunlola, O.A., Nunoo, S., Ateh, K.I., Elburg, M., Hofmann, A.,
37
38 733 2022. Crustal modelling from Pan-African granites of the Colomine Gold District, SE
39
40 734 Cameroon: Insights from zircon U-Pb dating and Lu-Hf isotope systematics. *Journal of*
41
42 735 *African Earth Sciences* 187, 104441. <https://doi.org/10.1016/j.jafrearsci.2021.104441>
43
44
45
- 46 736 Ngnotue, T., Ganno, S., Nzenti Jean, P., Schulz, B., Tchaptchet Tchato, D.I., Suh Cheo, E.,
47
48 737 2012. Geochemistry and Geochronology of Peraluminous High-K Granitic Leucosomes
49
50 738 of Yaoundé Series (Cameroon): Evidence for a Unique Pan-African Magmatism and
51
52 739 Melting Event in North Equatorial Fold Belt. *International Journal of Geosciences* 2012.
53
54 740 <https://doi.org/10.4236/ijg.2012.33055>
55
56
57
58
59
60
61
62
63
64
65

- 741 Niu, Y., Zhao, Z., Zhu, D.-C., Mo, X., 2013. Continental collision zones are primary sites for
1
2 742 net continental crust growth — A testable hypothesis. *Earth-Science Reviews* 127, 96–
3
4 743 110. <https://doi.org/10.1016/j.earscirev.2013.09.004>
5
6
7 744 Njanko, T., Nédélec, A., Affaton, P., 2006. Synkinematic high-K calc-alkaline plutons
8
9 745 associated with the Pan-African Central Cameroon shear zone (W-Tibati area):
10
11 746 Petrology and geodynamic significance. *Journal of African Earth Sciences, The*
12
13 747 *Precambrian of Central Africa* 44, 494–510.
14
15 748 <https://doi.org/10.1016/j.jafrearsci.2005.11.016>
16
17
18
19 749 Njiekak, G., Dörr, W., Tchouankoué, J.-P., Zulauf, G., 2008. U–Pb zircon and microfabric data
20
21 750 of (meta) granitoids of western Cameroon: Constraints on the timing of pluton
22
23 751 emplacement and deformation in the Pan-African belt of central Africa. *Lithos* 102,
24
25 752 460–477. <https://doi.org/10.1016/j.lithos.2007.07.020>
26
27
28
29 753 Nkoumbou, C., Barbey, P., Yonta-Ngouné, C., Paquette, J.L., Villiéras, F., 2014. Pre-
30
31 754 collisional geodynamic context of the southern margin of the Pan-African fold belt in
32
33 755 Cameroon. *Journal of African Earth Sciences* 99, 245–260.
34
35 756 <https://doi.org/10.1016/j.jafrearsci.2013.10.002>
36
37
38
39 757 Nomo, E.N., Tchameni, R., Vanderhaeghe, O., Sun, F., Barbey, P., Tekoum, L., Tchunte,
40
41 758 P.M.F., Eglinger, A., Fouotsa, N.A.S., 2017. Structure and LA-ICP-MS zircon U–Pb
42
43 759 dating of syntectonic plutons emplaced in the Pan-African Banyo-Tcholliré shear zone
44
45 760 (central north Cameroon). *Journal of African Earth Sciences* 131, 251–271.
46
47 761 <https://doi.org/10.1016/j.jafrearsci.2017.04.002>
48
49
50
51 762 Nomo Negue, E., Takodjou Wambo, J.D., Yamgouot Ngounouno, F., Negou Nembouet, J.,
52
53 763 Teda Soh, A.C., Tsassé Nganno, A.S., Fossi, D.H., Tchameni, R., 2021. Searching gold
54
55 764 origin through litho-structural analysis and morphological characterization of alluvial
56
57
58
59
60
61
62
63
64
65

765 gold nuggets in the Guiwa-Yangamo area (Batouri goldfield, Eastern Cameroon). Arab
1
2 766 J Geosci 14, 1973. <https://doi.org/10.1007/s12517-021-07799-5>
3
4
5 767 Nzenti, J.P., Barbey, P., Macaudiere, J., Soba, D., 1988. Origin and evolution of the late
6
7 768 precambrian high-grade Yaounde Gneisses (Cameroon). *Precambrian Research* 38, 91–
8
9 769 109. [https://doi.org/10.1016/0301-9268\(88\)90086-1](https://doi.org/10.1016/0301-9268(88)90086-1)
10
11 770 Owona, S., Ratschbacher, L., Nsangou Ngapna, M., Gulzar, A.M., Mvondo Ondo, J.,
12
13 771 Emmanuel Ekodeck, G., 2021a. How diverse is the source? Age, provenance,
14
15 772 reworking, and overprint of Precambrian meta-sedimentary rocks of West Gondwana,
16
17 773 Cameroon, from zircon U-Pb geochronology. *Precambrian Research* 359, 106220.
18
19 774 <https://doi.org/10.1016/j.precamres.2021.106220>
20
21 775 Owona, S., Ratschbacher, L., Nsangou Ngapna, M., Gulzar, A.M., Mvondo Ondo, J.,
22
23 776 Emmanuel Ekodeck, G., 2021b. How diverse is the source? Age, provenance,
24
25 777 reworking, and overprint of Precambrian meta-sedimentary rocks of West Gondwana,
26
27 778 Cameroon, from zircon U-Pb geochronology. *Precambrian Research* 359, 106220.
28
29 779 <https://doi.org/10.1016/j.precamres.2021.106220>
30
31 780 Owona, S., Schulz, B., Ratschbacher, L., Mvondo Ondo, J., Ekodeck, G.E., Tchoua, F.M.,
32
33 781 Affaton, P., 2011. Pan-African metamorphic evolution in the southern Yaounde Group
34
35 782 (Oubanguide Complex, Cameroon) as revealed by EMP-monazite dating and
36
37 783 thermobarometry of garnet metapelites. *Journal of African Earth Sciences* 59, 125–139.
38
39 784 <https://doi.org/10.1016/j.jafrearsci.2010.09.003>
40
41 785 Owona, S., Tichomirowa, M., Ratschbacher, L., Ondo, J.M., Youmen, D., Pfänder, J., Tchoua,
42
43 786 F.M., Affaton, P., Ekodeck, G.E., 2012. New igneous zircon Pb/Pb and metamorphic
44
45 787 Rb/Sr ages in the Yaounde Group (Cameroon, Central Africa): implications for the
46
47 788 Central African fold belt evolution close to the Congo Craton. *Int J Earth Sci (Geol*
48
49 789 *Rundsch)* 101, 1689–1703. <https://doi.org/10.1007/s00531-012-0751-x>
50
51
52
53
54
55
56
57
58
59
60
61
62
63
64
65

- 790 Paquette, J.-L., Piro, J.-L., Devidal, J.-L., Bosse, V., Didier, A., Sannac, S., Abdelnour, Y.,
1
2 791 2014. Sensitivity enhancement in LA-ICP-MS by N₂ addition to carrier gas: application
3
4 792 to radiometric dating of U-Th-bearing minerals. *Agilent ICP-MS Journal* 58, 4–5.
5
6
7 793 Parrish, R.R., 1990. U–Pb dating of monazite and its application to geological problems. *Can.*
8
9 794 *J. Earth Sci.* 27, 1431–1450. <https://doi.org/10.1139/e90-152>
10
11 795 Paton, C., Woodhead, J.D., Hellstrom, J.C., Hergt, J.M., Greig, A., Maas, R., 2010. Improved
12
13 796 laser ablation U-Pb zircon geochronology through robust downhole fractionation
14
15 797 correction: IMPROVED LASER ABLATION U-Pb GEOCHRONOLOGY. *Geochem.*
16
17 798 *Geophys. Geosyst.* 11, n/a-n/a. <https://doi.org/10.1029/2009GC002618>
18
19
20
21 799 Paul, A., Jung, S., Romer, R.L., Stracke, A., Hauff, F., 2014. Petrogenesis of synorogenic high-
22
23 800 temperature leucogranites (Damara orogen, Namibia): Constraints from U–Pb monazite
24
25 801 ages and Nd, Sr and Pb isotopes. *Gondwana Research* 25, 1614–1626.
26
27 802 <https://doi.org/10.1016/j.gr.2013.06.008>
28
29
30
31 803 Pearce, J.A., 2008. Geochemical fingerprinting of oceanic basalts with applications to ophiolite
32
33 804 classification and the search for Archean oceanic crust. *Lithos* 100, 14–48.
34
35 805 <https://doi.org/10.1016/j.lithos.2007.06.016>
36
37
38 806 Pearce, J.A., Harris, N.B.W., Tindle, A.G., 1984. Trace Element Discrimination Diagrams for
39
40 807 the Tectonic Interpretation of Granitic Rocks. *Journal of Petrology* 25, 956–983.
41
42 808 <https://doi.org/10.1093/petrology/25.4.956>
43
44
45 809 Peccerillo, A., Taylor, S.R., 1976. Geochemistry of eocene calc-alkaline volcanic rocks from
46
47 810 the Kastamonu area, Northern Turkey. *Contr. Mineral. and Petrol.* 58, 63–81.
48
49 811 <https://doi.org/10.1007/BF00384745>
50
51
52 812 Penaye, J., Kröner, A., Toteu, S.F., Van Schmus, W.R., Doumnang, J.-C., 2006. Evolution of
53
54 813 the Mayo Kebbi region as revealed by zircon dating: An early (ca. 740Ma) Pan-African
55
56 814 magmatic arc in southwestern Chad. *Journal of African Earth Sciences*, The
57
58
59
60
61
62
63
64
65

1
2
3
4
5
6
7
8
9
10
11
12
13
14
15
16
17
18
19
20
21
22
23
24
25
26
27
28
29
30
31
32
33
34
35
36
37
38
39
40
41
42
43
44
45
46
47
48
49
50
51
52
53
54
55
56
57
58
59
60
61
62
63
64
65

815 Precambrian of Central Africa 44, 530–542.
816 <https://doi.org/10.1016/j.jafrearsci.2005.11.018>
817 Penaye, J., Toteu, S.F., Van Schmus, W.R., Nzenti, J.-P., 1993. U-Pb and Sm-Nd preliminary
818 geochronologic data on the Yaounde Series, Cameroon: re-interpretation of the
819 granulitic rocks as the suture of a collision in the "Centrafrican' belt. *Comptes Rendus*
820 - Academie des Sciences, Serie II 317, 789–794.
821 Polat, A., Hofmann, A.W., 2003. Alteration and geochemical patterns in the 3.7–3.8 Ga Isua
822 greenstone belt, West Greenland. *Precambrian Research* 126, 197–218.
823 [https://doi.org/10.1016/S0301-9268\(03\)00095-0](https://doi.org/10.1016/S0301-9268(03)00095-0)
824 Rapp, R.P., Shimizu, N., Norman, M.D., Applegate, G.S., 1999. Reaction between slab-derived
825 melts and peridotite in the mantle wedge: experimental constraints at 3.8 GPa. *Chemical*
826 *Geology* 160, 335–356. [https://doi.org/10.1016/S0009-2541\(99\)00106-0](https://doi.org/10.1016/S0009-2541(99)00106-0)
827 Rogers, J.J.W., Greenberg, J.K., 1990. Late-Orogenic, Post-Orogenic, and Anorogenic
828 Granites: Distinction by Major-Element and Trace-Element Chemistry and Possible
829 Origins. *The Journal of Geology* 98, 291–309. <https://doi.org/10.1086/629406>
830 Rollinson, H., Pease, V., 2021. Using geochemical data to solve geological problems.
831 Saha-Fouotsa, A.N., Vanderhaeghe, O., Barbey, P., Eglinger, A., Tchameni, R., Zeh, A.,
832 Tchunte, P.F., Nomo, E.N., 2019. The geologic record of the exhumed root of the
833 Central African Orogenic Belt in the central Cameroon domain (Mbé – Sassa-Mbersi
834 region). *Journal of African Earth Sciences* 151, 286–314.
835 <https://doi.org/10.1016/j.jafrearsci.2018.12.008>
836 Saunders, A.D., Norry, M.J., Tarney, J., 1988. Origin of MORB and Chemically-Depleted
837 Mantle Reservoirs: Trace Element Constraints. *Journal of Petrology Special_Volume*,
838 415–445. https://doi.org/10.1093/petrology/Special_Volume.1.415

- 839 Schiano, P., Monzier, M., Eissen, J.-P., Martin, H., Koga, K.T., 2010. Simple mixing as the
1
2 840 major control of the evolution of volcanic suites in the Ecuadorian Andes. *Contrib*
3
4 841 *Mineral Petrol* 160, 297–312. <https://doi.org/10.1007/s00410-009-0478-2>
5
6
7 842 Schulz, B., 2021a. Petrochronology of Monazite-Bearing Garnet Micaschists as a Tool to
8
9 843 Decipher the Metamorphic Evolution of the Alpine Basement. *Minerals* 11, 981.
10
11 844 <https://doi.org/10.3390/min11090981>
12
13
14 845 Schulz, B., 2021b. Monazite Microstructures and Their Interpretation in Petrochronology.
15
16 846 *Front. Earth Sci.* 9, 668566. <https://doi.org/10.3389/feart.2021.668566>
17
18
19 847 Schulz, B., Krause, J., Zimmermann, R., 2019. Electron microprobe petrochronology of
20
21 848 monazite-bearing garnet micaschists in the Oetztal-Stubai Complex (Alpeiner Valley,
22
23 849 Stubai). *Swiss J Geosci* 112, 597–617. <https://doi.org/10.1007/s00015-019-00351-4>
24
25
26 850 Schulz, B., Schüssler, U., 2013. Electron-microprobe Th–U–Pb monazite dating in Early-
27
28 851 Palaeozoic high-grade gneisses as a completion of U–Pb isotopic ages (Wilson Terrane,
29
30 852 Antarctica). *Lithos* 175–176, 178–192. <https://doi.org/10.1016/j.lithos.2013.05.008>
31
32
33
34 853 Şengör, A.M.C., Cin, A., Rowley, D.B., Shangyou, N., 1991. Magmatic evolution of the
35
36 854 Tethysides: a guide to reconstruction of collage history. *Palaeogeography,*
37
38 855 *Palaeoclimatology, Palaeoecology, Palaeogeography and Paleoceanography of Tethys*
39
40 856 87, 411–440. [https://doi.org/10.1016/0031-0182\(91\)90143-F](https://doi.org/10.1016/0031-0182(91)90143-F)
41
42
43 857 Şengör, A.M.C., Natal'in, B.A., Sunal, G., Van Der Voo, R., 2018. The Tectonics of the
44
45 858 Altaids: Crustal Growth During the Construction of the Continental Lithosphere of
46
47 859 Central Asia Between ~750 and ~130 Ma Ago. *Annu. Rev. Earth Planet. Sci.* 46, 439–
48
49 860 494. <https://doi.org/10.1146/annurev-earth-060313-054826>
50
51
52
53 861 Shand, S., S.J., 1943. *Eruptive Rocks: Their Genesis. Composition, Classification, and Their*
54
55 862 *Relation to Ore Deposits with a Chapter on Meteorites.*
56
57
58
59
60
61
62
63
64
65

- 863 Simon, I., Jung, S., Romer, R.L., Garbe-Schönberg, D., Berndt, J., 2017. Geochemical and Nd-
1
2 864 Sr-Pb isotope characteristics of synorogenic lower crust-derived granodiorites (Central
3
4
5 865 Damara orogen, Namibia). *Lithos* 274–275, 397–411.
6
7 866 <https://doi.org/10.1016/j.lithos.2016.12.033>
8
9
10 867 Smithies, R.H., 2000. The Archaean tonalite–trondhjemite–granodiorite (TTG) series is not an
11
12 868 analogue of Cenozoic adakite. *Earth and Planetary Science Letters* 182, 115–125.
13
14 869 [https://doi.org/10.1016/S0012-821X\(00\)00236-3](https://doi.org/10.1016/S0012-821X(00)00236-3)
15
16
17 870 Soba, D., 1991. U-Pb, SmNd and Rb-Sr dating in the Pan-African Mobile Belt of Eastern
18
19 871 Cameroon: Upper Proterozoic age of the Lom series. *Comptes Rendus de l'Academie*
20
21 872 *des Sciences, Paris, Serie II. Sciences de la Terre et des Planetes* 312, 1453–1458.
22
23
24 873 Sun, G., Liu, S., Cawood, P.A., Tang, M., van Hunen, J., Gao, L., Hu, Y., Hu, F., 2021. Thermal
25
26 874 state and evolving geodynamic regimes of the Meso- to Neoproterozoic North China
27
28 875 Craton. *Nat Commun* 12, 3888. <https://doi.org/10.1038/s41467-021-24139-z>
29
30
31 876 Sun, S. -s., McDonough, W.F., 1989. Chemical and isotopic systematics of oceanic basalts:
32
33 877 implications for mantle composition and processes. Geological Society, London,
34
35 878 *Special Publications* 42, 313–345. <https://doi.org/10.1144/GSL.SP.1989.042.01.19>
36
37
38
39 879 Suzuki, K., Adachi, M., Kajizuka, I., 1994. Electron microprobe observations of Pb diffusion
40
41 880 in metamorphosed detrital monazites. *Earth and Planetary Science Letters* 128, 391–
42
43 881 405. [https://doi.org/10.1016/0012-821X\(94\)90158-9](https://doi.org/10.1016/0012-821X(94)90158-9)
44
45
46 882 Suzuki, K., Kato, T., 2008. CHIME dating of monazite, xenotime, zircon and polycrase:
47
48 883 Protocol, pitfalls and chemical criterion of possibly discordant age data. *Gondwana*
49
50 884 *Research* 14, 569–586. <https://doi.org/10.1016/j.gr.2008.01.005>
51
52
53 885 Sylvester, P.J., 1998. Post-collisional strongly peraluminous granites. *Lithos* 45, 29–44.
54
55 886 [https://doi.org/10.1016/S0024-4937\(98\)00024-3](https://doi.org/10.1016/S0024-4937(98)00024-3)
56
57
58
59
60
61
62
63
64
65

- 887 Tchakounté, J., Eglinger, A., Toteu, S.F., Zeh, A., Nkoumbou, C., Mvondo-Ondoa, J., Penaye,
1
2 888 J., De Wit, M., Barbey, P., 2017. The Adamawa-Yadé domain, a piece of Archaean
3
4 889 crust in the Neoproterozoic Central African Orogenic belt (Bafia area, Cameroon).
5
6
7 890 Precambrian Research 299, 210–229. <https://doi.org/10.1016/j.precamres.2017.07.001>
8
9
10 891 Tchameni, R., Pouclet, A., Penaye, J., Ganwa, A.A., Toteu, S.F., 2006. Petrography and
11
12 892 geochemistry of the Ngaoundéré Pan-African granitoids in Central North Cameroon:
13
14 893 Implications for their sources and geological setting. Journal of African Earth Sciences,
15
16
17 894 The Precambrian of Central Africa 44, 511–529.
18
19 895 <https://doi.org/10.1016/j.jafrearsci.2005.11.017>
20
21
22 896 Thieblemont, D., Tegye, M., 1994. Geochemical discrimination of differentiated magmatic
23
24 897 rocks attesting for the variable origin and tectonic setting of calc-alkaline magmas.
25
26 898 Comptes Rendus De L Academie Des Sciences Serie II 319, 87–94.
27
28
29 899 Toteu, S.F., de Wit, M., Penaye, J., Drost, K., Tait, J.A., Bouyo, M.H., Van Schmus, W.R.,
30
31 900 Jelsma, H., Moloto-A-Kenguemba, G.R., da Silva Filho, A.F., Lerouge, C., Doucouré,
32
33
34 901 M., 2022. Geochronology and correlations in the Central African Fold Belt along the
35
36 902 northern edge of the Congo Craton: New insights from U-Pb dating of zircons from
37
38
39 903 Cameroon, Central African Republic, and south-western Chad. Gondwana Research
40
41 904 107, 296–324. <https://doi.org/10.1016/j.gr.2022.03.010>
42
43
44 905 Toteu, S.F., Penaye, J., Deloule, E., Van Schmus, W.R., Tchameni, R., 2006. Diachronous
45
46 906 evolution of volcano-sedimentary basins north of the Congo craton: Insights from U–
47
48 907 Pb ion microprobe dating of zircons from the Poli, Lom and Yaoundé Groups
49
50
51 908 (Cameroon). Journal of African Earth Sciences 44, 428–442.
52
53 909 <https://doi.org/10.1016/j.jafrearsci.2005.11.011>
54
55
56
57
58
59
60
61
62
63
64
65

- 910 Toteu, S.F., Penaye, J., Djomani, Y.P., 2004. Geodynamic evolution of the Pan-African belt in
1
2 911 central Africa with special reference to Cameroon. *Can. J. Earth Sci.* 41, 73–85.
3
4 912 <https://doi.org/10.1139/e03-079>
5
6
7 913 Toteu, S.F., Van Schmus, W.R., Penaye, J., Michard, A., 2001. New U–Pb and Sm–Nd data
8
9 914 from north-central Cameroon and its bearing on the pre-Pan African history of central
10
11 915 Africa. *Precambrian Research* 108, 45–73. <https://doi.org/10.1016/S0301->
12
13 916 [9268\(00\)00149-2](https://doi.org/10.1016/S0301-9268(00)00149-2)
14
15
16
17 917 Toteu, S.F., Van Schmus, W.R., Penaye, J., Nyobé, J.B., 1994. U–Pb and Sm–Nd evidence
18
19 918 for Eburnian and Pan-African high-grade metamorphism in cratonic rocks of southern
20
21 919 Cameroon. *Precambrian Research* 67, 321–347. <https://doi.org/10.1016/0301->
22
23 920 [9268\(94\)90014-0](https://doi.org/10.1016/0301-9268(94)90014-0)
24
25
26
27 921 Trompette, R., 1997. Neoproterozoic (~600 Ma) aggregation of Western Gondwana: a tentative
28
29 922 scenario. *Precambrian Research* 82, 101–112. <https://doi.org/10.1016/S0301->
30
31 923 [9268\(96\)00045-9](https://doi.org/10.1016/S0301-9268(96)00045-9)
32
33
34 924 Vermeesch, P., 2018. IsoplotR: A free and open toolbox for geochronology. *Geoscience*
35
36 925 *Frontiers* 9, 1479–1493. <https://doi.org/10.1016/j.gsf.2018.04.001>
37
38
39 926 Wang, T., Tong, Y., Huang, H., Zhang, H., Guo, L., Li, Z., Wang, X., Eglington, B., Li, S.,
40
41 927 Zhang, J., Donskaya, T.V., Petrov, O., Zhang, L., Song, P., Zhang, X., Wang, C., 2023.
42
43 928 Granitic record of the assembly of the Asian continent. *Earth-Science Reviews* 237,
44
45 929 [104298. https://doi.org/10.1016/j.earscirev.2022.104298](https://doi.org/10.1016/j.earscirev.2022.104298)
46
47
48
49 930 Weaver, B.L., 1991. The origin of ocean island basalt end-member compositions: trace element
50
51 931 and isotopic constraints. *Earth and Planetary Science Letters* 104, 381–397.
52
53 932 [https://doi.org/10.1016/0012-821X\(91\)90217-6](https://doi.org/10.1016/0012-821X(91)90217-6)
54
55
56
57
58
59
60
61
62
63
64
65

- 933 Whalen, J.B., Currie, K.L., Chappell, B.W., 1987. A-type granites: geochemical characteristics,
1
2 934 discrimination and petrogenesis. *Contrib Mineral Petrol* 95, 407–419.
3
4 935 <https://doi.org/10.1007/BF00402202>
6
- 7 936 Wiedenbeck, M., Allé, P., Corfu, F., Griffin, W.L., Meier, M., Oberli, F., Quadt, A.V., Roddick,
8
9 937 J.C., Spiegel, W., 1995. THREE NATURAL ZIRCON STANDARDS FOR U-TH-PB,
10
11 938 LU-HF, TRACE ELEMENT AND REE ANALYSES. *Geostandards and Geoanalytical*
13
14 939 *Research* 19, 1–23. <https://doi.org/10.1111/j.1751-908X.1995.tb00147.x>
15
16
- 17 940 Williams, M.L., Jercinovic, M.J., Harlov, D.E., Budzyń, B., Hetherington, C.J., 2011. Resetting
18
19 941 monazite ages during fluid-related alteration. *Chemical Geology* 283, 218–225.
20
21 942 <https://doi.org/10.1016/j.chemgeo.2011.01.019>
23
- 24 943 Williams, M.L., Jercinovic, M.J., Mahan, K.H., Dumond, G., 2017. 5. Electron Microprobe
25
26 944 Petrochronology, in: Kohn, M.J., Engi, M., Lanari, P. (Eds.), *Petrochronology*. De
27
28 945 Gruyter, Berlin, Boston. <https://doi.org/10.1515/9783110561890-006>
30
- 31 946 Wu, F., Liu, X., Ji, W., Wang, J., Yang, L., 2017. Highly fractionated granites: Recognition and
32
33 947 research. *Sci. China Earth Sci.* 60, 1201–1219. <https://doi.org/10.1007/s11430-016->
34
35 948 5139-1
37
- 38 949 Wu, Y., Zheng, Y., 2004. Genesis of zircon and its constraints on interpretation of U-Pb age.
40
41 950 *Chin.Sci.Bull.* 49, 1554–1569. <https://doi.org/10.1007/BF03184122>
42
- 43 951 Yonta-Ngoune, C., Nkoumbou, C., Barbey, P., Le Breton, N., Montel, J.-M., Villieras, F., 2010.
44
45 952 Geological context of the Boumnyebel talcschists (Cameroun): Inferences on the Pan-
46
47 953 African Belt of Central Africa. *Comptes Rendus Geoscience* 342, 108–115.
48
49 954 <https://doi.org/10.1016/j.crte.2009.12.007>
50
51 955
52
- 53 956 Zhu, D., Mo, X., Wang, L., Zhao, Z., Niu, Y., Zhou, C., Yang, Y., 2009. Petrogenesis of highly
54
55 956 fractionated I-type granites in the Zayu area of eastern Gangdese, Tibet: Constraints
56
57
58
59
60
61
62
63
64
65

957	from zircon U-Pb geochronology, geochemistry and Sr-Nd-Hf isotopes. Sci. China Ser.
1	
2 958	D-Earth Sci. 52, 1223–1239. https://doi.org/10.1007/s11430-009-0132-x
3	
4	
5 959	
6	
7	
8 960	
9	
10	
11 961	
12	
13	
14 962	
15	
16	
17 963	
18	
19	
20 964	
21	
22	
23 965	
24	
25	
26 966	
27	
28	
29	
30 967	
31	
32	
33 968	
34	
35	
36 969	
37	
38	
39 970	
40	
41	
42 971	
43	
44	
45 972	
46	
47	
48 973	
49	
50	
51 974	
52	
53	
54 975	
55	
56	
57 976	
58	
59	
60	
61	
62	
63	
64	
65	

977 **Figure captions**

1
2
3 978 **Fig. 1.** a) General geological map of Cameroon comprising different tectonic units separated
4
5 979 by major thrust-fault. Inset shows a reconstruction of the West Gondwana. b) Map of the study
6
7
8 980 area showing sample locations (modified after Gazel and Gérard (1954)).
9

10 981 **Fig. 2.** Field and petrographic photographs of the studied Neoproterozoic granites in the Gari-
11
12 982 Gombo area. Mineral abbreviations: Qtz, quartz; Kfs- K-feldspar; Pl, plagioclase; Bt, biotite;
13
14
15 983 Zr, zircon; and Chl, chlorite. Red arrows indicate dynamic micro-recrystallization of quartz.
16
17

18 984 **Fig. 3. (a-b)** Cathodoluminescence images of zircons in the analysed samples from the Gari-
19
20
21 985 Gombo granite. **(c-d)** Zircon U–Pb concordia diagrams, upper intercept ages, and weighted
22
23 986 mean $^{206}\text{Pb}/^{238}\text{U}$ ages of samples from the study samples.
24
25

26 987 **Fig. 4.** BSE images of selected monazite grains and monazite mineral in sample GB4. Dated
27
28
29 988 spots with weighted mean EPMA ages (in Ma) of grain are indicated. a) Large monazite with
30
31 989 oscillatory zonations. b) Small grain with distinct sector zoning. c) large grain with igneous Th-
32
33
34 990 rich domains (bright) and slightly (grey) and strongly altered (patchy) domains. d) Igneous
35
36 991 monazite with domains of alteration (black dots). Dated spots with single date (in Ma), and with
37
38
39 992 weighted mean EPMA ages (in Ma) of grains are indicated. e) Potential regression of age vs
40
41 993 ThO_2 in > 605 and < 605 monazite analyses. f) Th+U vs Ca of > 605 and > 605 Ma monazite
42
43 994 analyses in sample GB4.
44

45 995 **Fig. 5.** Th–U–Pb chemical model ages of monazite (Mnz). **a)** Total ThO_2^* vs PbO (wt%)
46
47
48 996 isochrons diagrams. ThO_2^* is $\text{ThO}_2 + \text{UO}_2$ equivalents expressed as ThO_2 . General minimal 2σ
49
50
51 997 error on monazite PbO analysis is shown by a bar. Regression lines with the coefficient of
52
53 998 determination R^2 are forced through zero (Montel et al., 1996; Suzuki et al., 1994). **b)** Weighted
54
55
56 999 average ages in Ma with MSWD and minimal error of 2σ are calculated from the single analyses
57
581000 belonging to an isochrone according to Ludwig (2009).
59
60
61
62
63
64
65

1001 **Fig. 6.** Geochemistry of the Gari-Gombo granite. (a) TAS diagram (after Middlemost 1994)
1
2 1002 showing chemical composition of the granite. (b) SiO₂ vs. K₂O plot (after Peccerillo and Taylor
3
4 1003 1976). (c) Plot of FeOt/(FeOt + MgO) vs. SiO₂ (after Frost et al. 2001). (d) Alumina saturation
5
6
7 1004 index diagram for the Gari-Gombo granitoids (after Shand, 1943). Ternary classification
8
9
10 1005 diagram for granitoids: 2*A/CNK (molar Al₂O₃/[CaO+ Na₂O + K₂O] ratio)-Na₂O/K₂O ratio-
11
12 1006 2FMSB) (after Laurent et al., 2014).-(f) Ce (ppm) vs SiO₂ (wt. %) plot of Whalen et al. (1987),
13
14 1007 showing granitic samples from Gari-Gombo pluton are mainly I-type granites.
15

16
17 1008 **Fig. 7.** REE and trace element patterns for the Gari-Gombo granite. (a) Chondrite normalized
18
19 1009 REE plots normalizing values are from Anders and Grevesse, (1989). (b) primitive-mantle
20
21
22 1010 normalized multi-elemental variation diagrams respectively for the Gari-Gombo granite
23
24 1011 (Normalizing values from Sun and McDonough 1989).
25

26
27 1012 **Fig. 8.** (a) (Al₂O₃+CaO)/(FeOt+Na₂O+K₂O) vs 100*(MgO+FeOt+TiO₂)/SiO₂ diagrams for
28
29
30 1013 Gari-Gombo granite (after Sylvester, 1998). b) Rb/S vs Rb(ppm) diagrams (after Sun et al.,
31
32 1014 2021). (c) Al₂O₃/(FeOt + MgO)-3*CaO-5*(K₂O/Na₂O) ternary diagram (after Laurent et al.
33
34 1015 2014). (d) Rb/Ba versus Rb/Sr (c, d) for Neoproterozoic granite of Gari-Gombo area. calculated
35
36
37 1016 pelite- and greywacke-derived melts are from Sylvester (1998). e) Plot of Ba (ppm) vs. Sr (ppm)
38
39 1017 concentrations (b) Plot of Rb (ppm) vs. Sr (ppm) concentrations from the Gari-Gombo granites
40
41
42 1018 to show the effects of fractional crystallization processes. Mineral vectors calculated according
43
44 1019 to partition coefficients from (Ewart and Griffin, 1994).
45

46
47 1020 **Fig. 9.** (a-b) Discrimination of melt sources (based on Moyen et al. (2017) and Eby (1992)).
48
49 1021 (c-f) Discrimination of tectonic position of the Gari-Gombo granites (Batchelor and Bowden,
50
51 1022 1985; Pearce et al., 1984).
52

53
54 1023
55
56
57 1024
58
59
60 1025
61

1026 **Tables**

1

2

31027 Table 1. U-Pb zircon data from samples GB1 and GB4 (Gari-Gombo granites).

4

5

61028 Table 2. Selected electron microprobe analyses of monazite from granite (sample GB4) of Gari-

7

81029 Gombo area

9

101030 Table 3. Major oxides (in wt%) and trace element (in ppm) compositions for the Gari-Gombo

11

121031 granites.

13

14

15

16

17

18

19

20

21

22

23

24

25

26

27

28

29

30

31

32

33

34

35

36

37

38

39

40

41

42

43

44

45

46

47

48

49

50

51

52

53

54

55

56

57

58

59

60

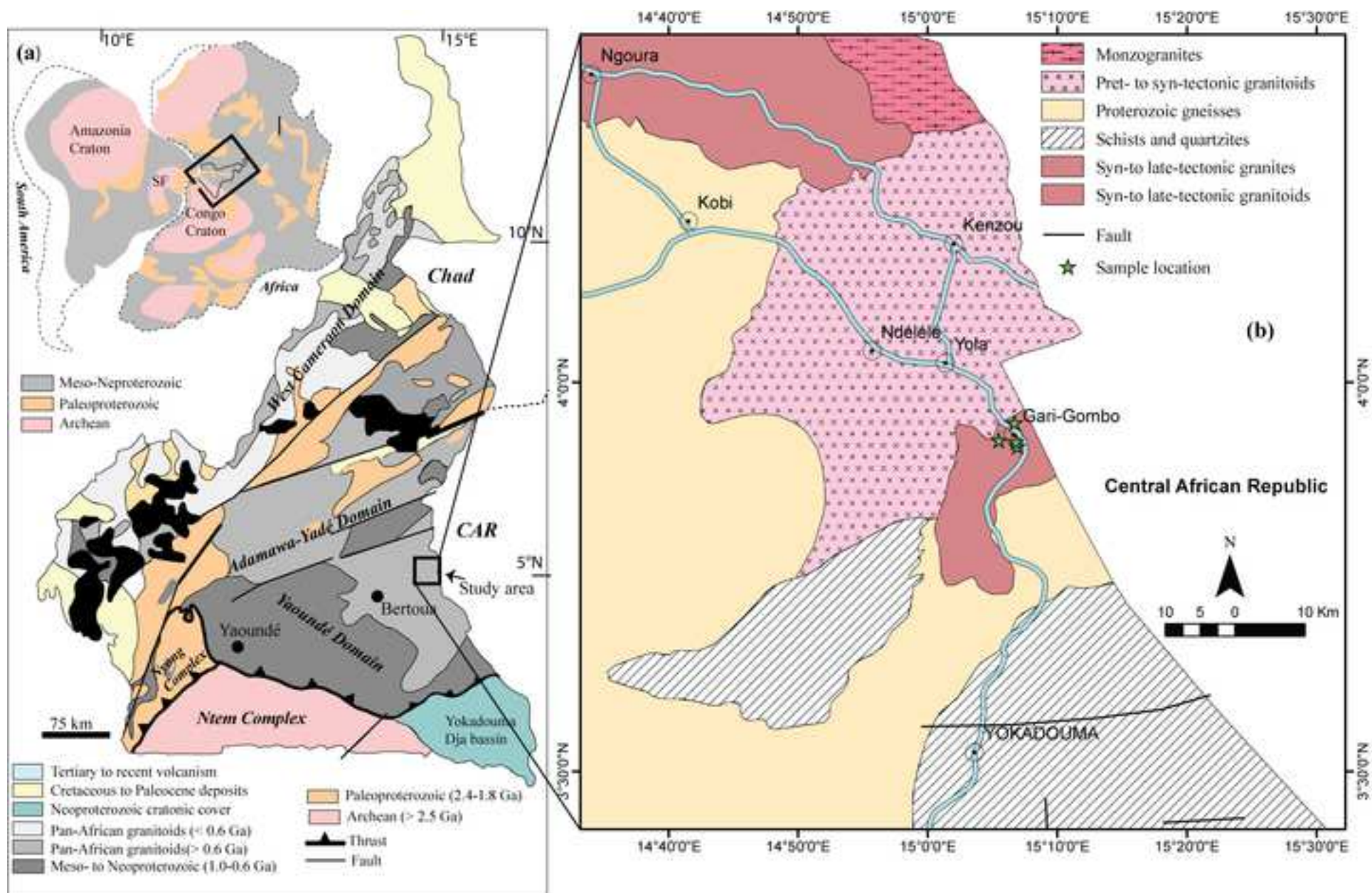
61

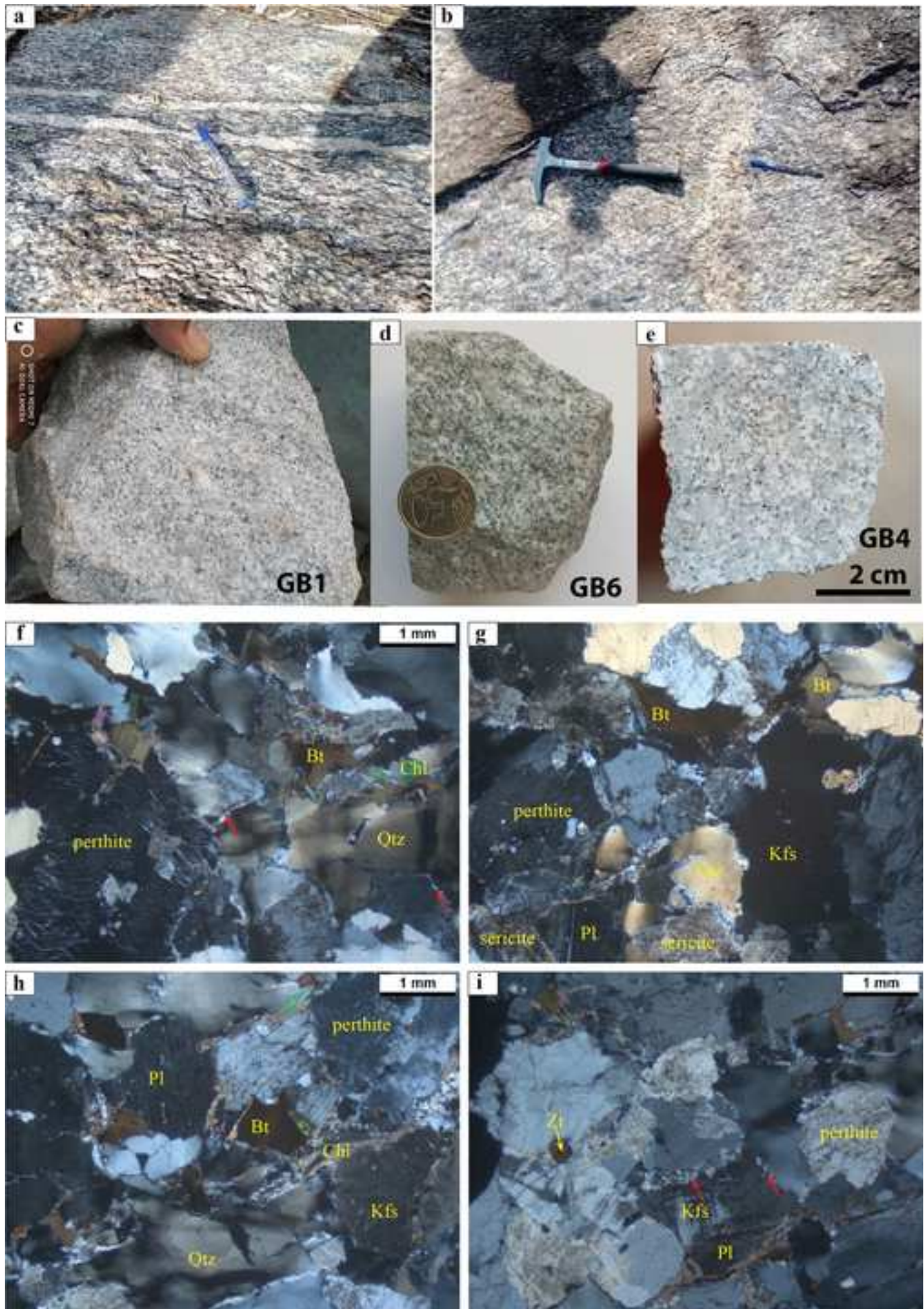
62

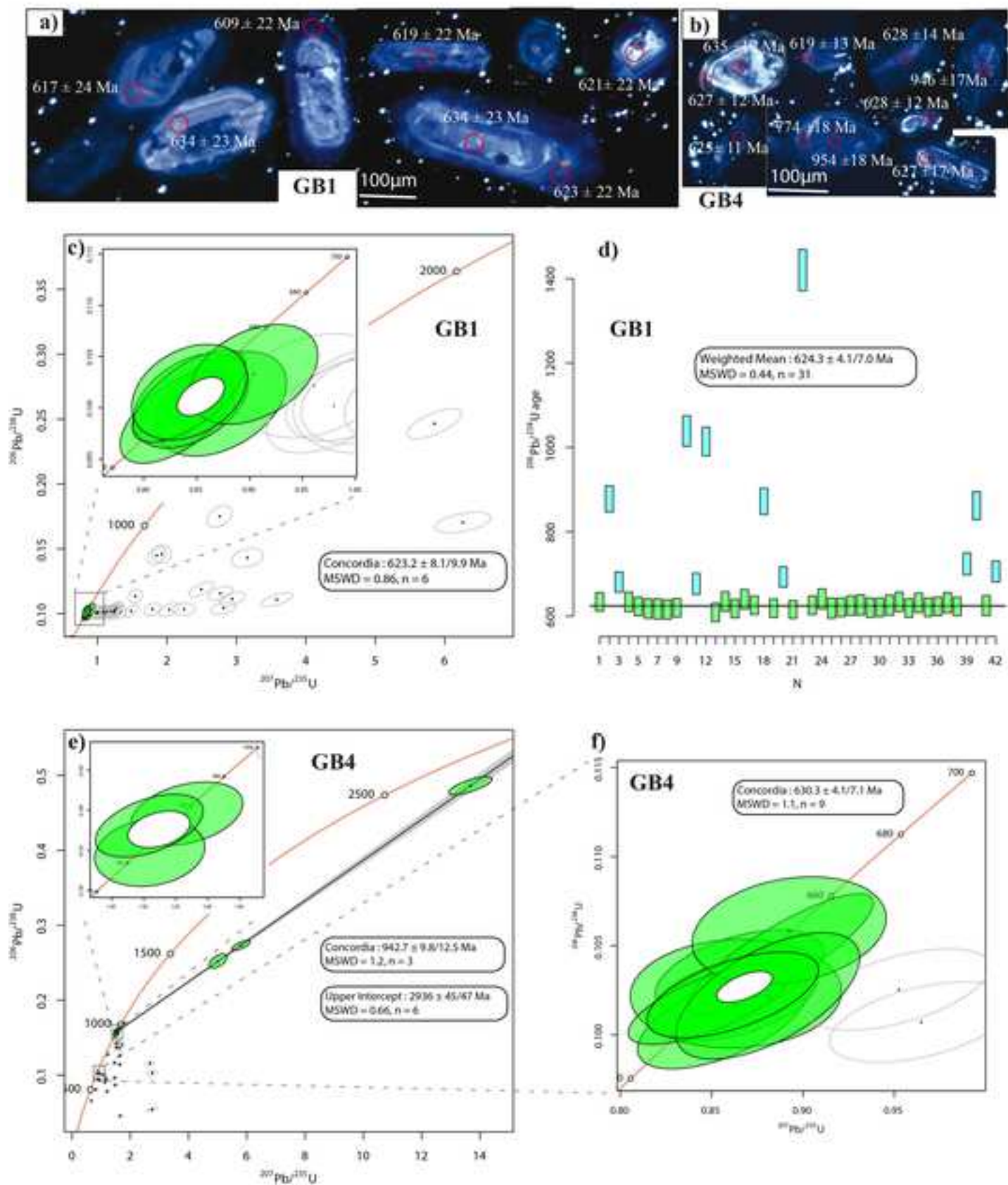
63

64

65







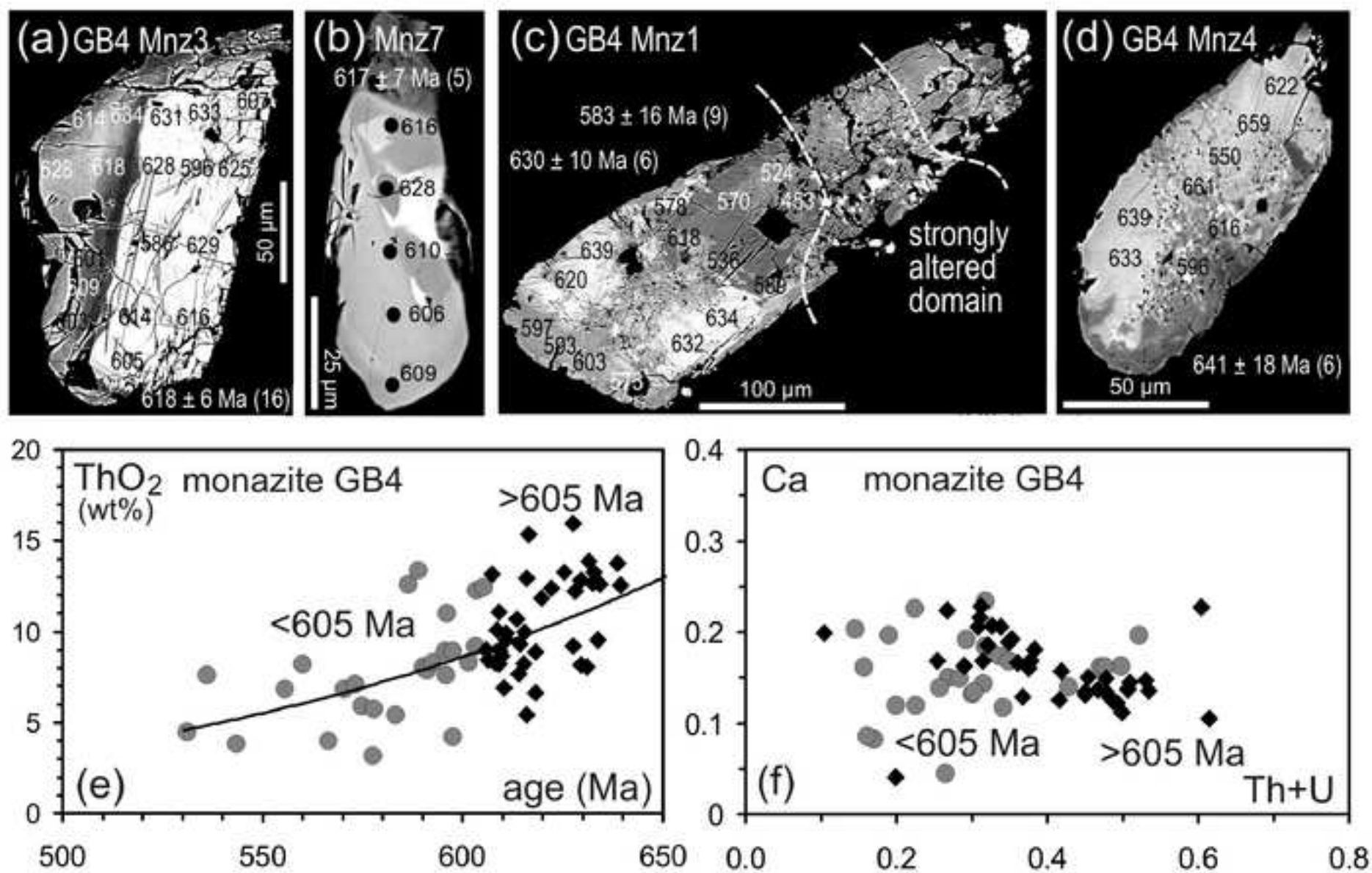
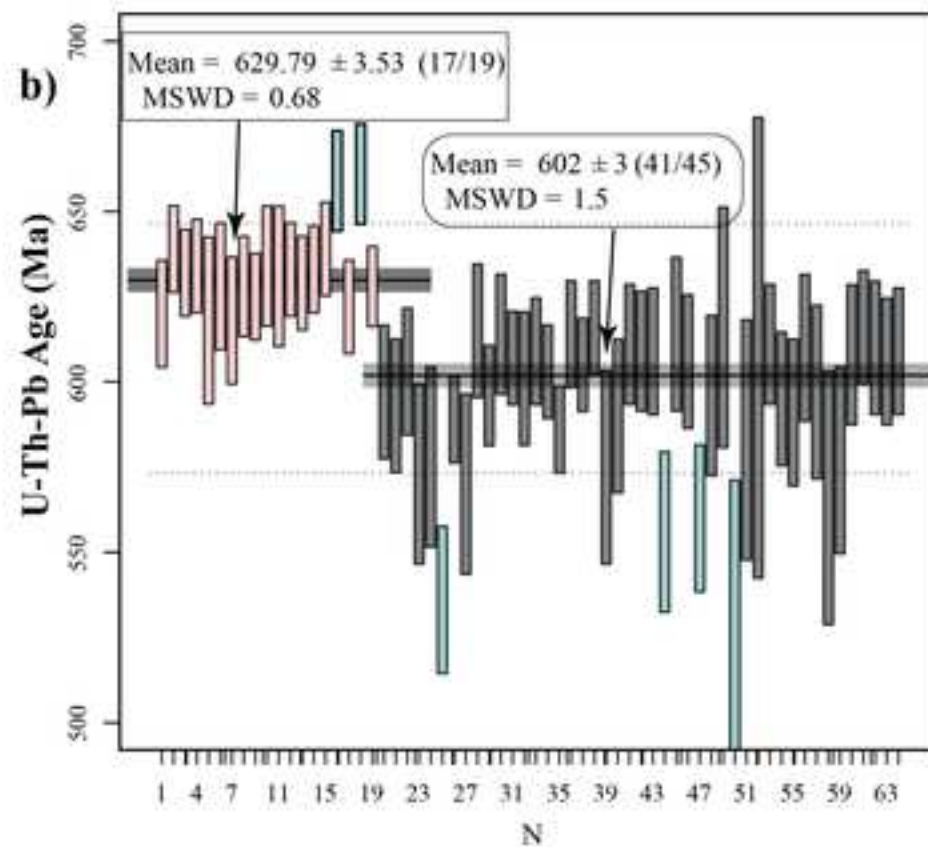
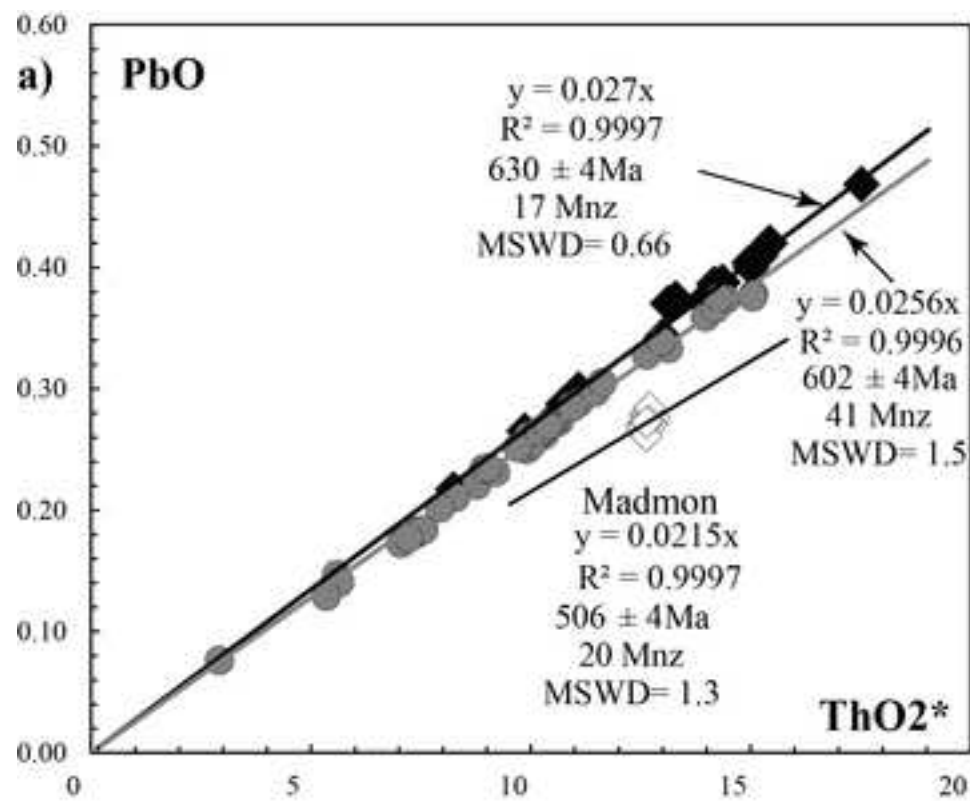
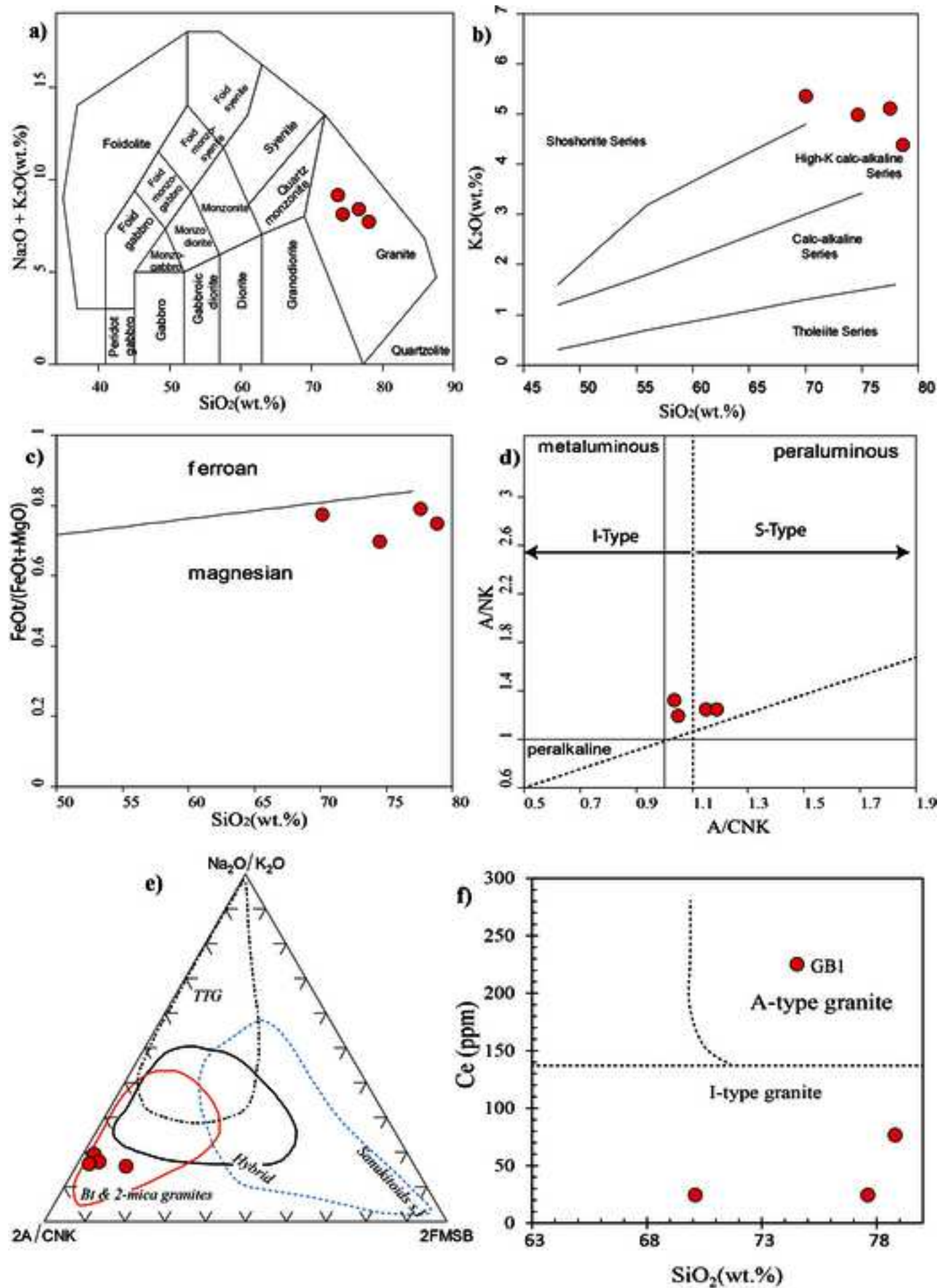
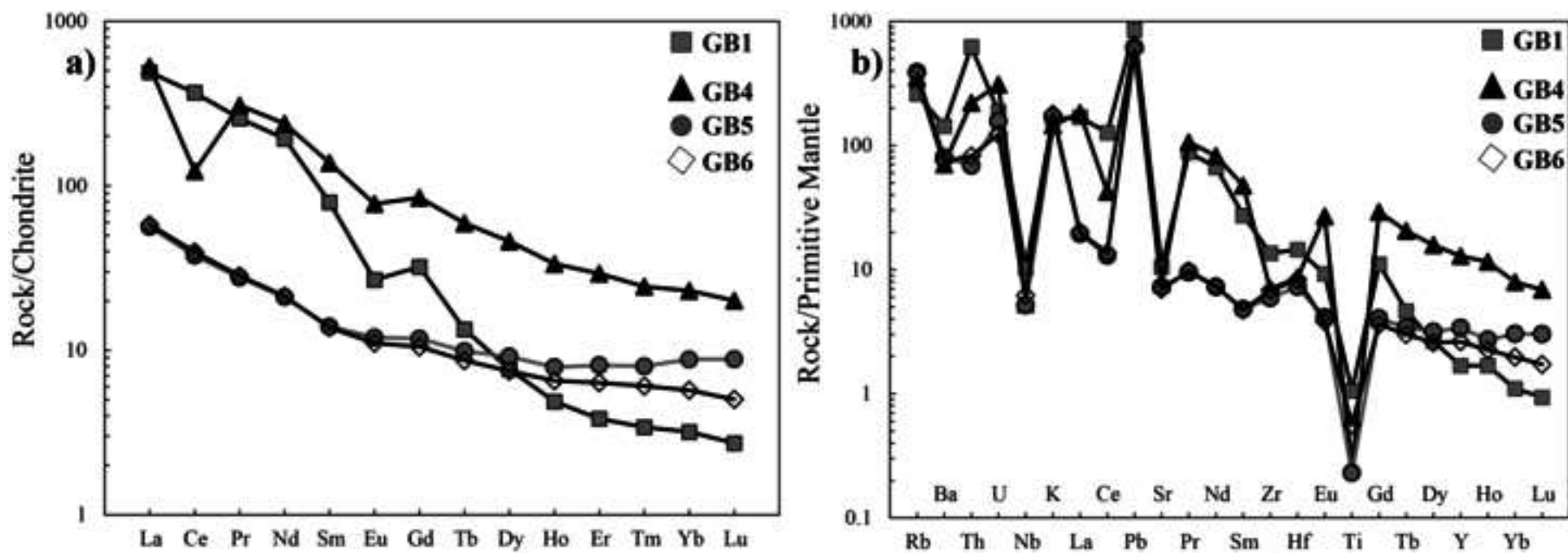
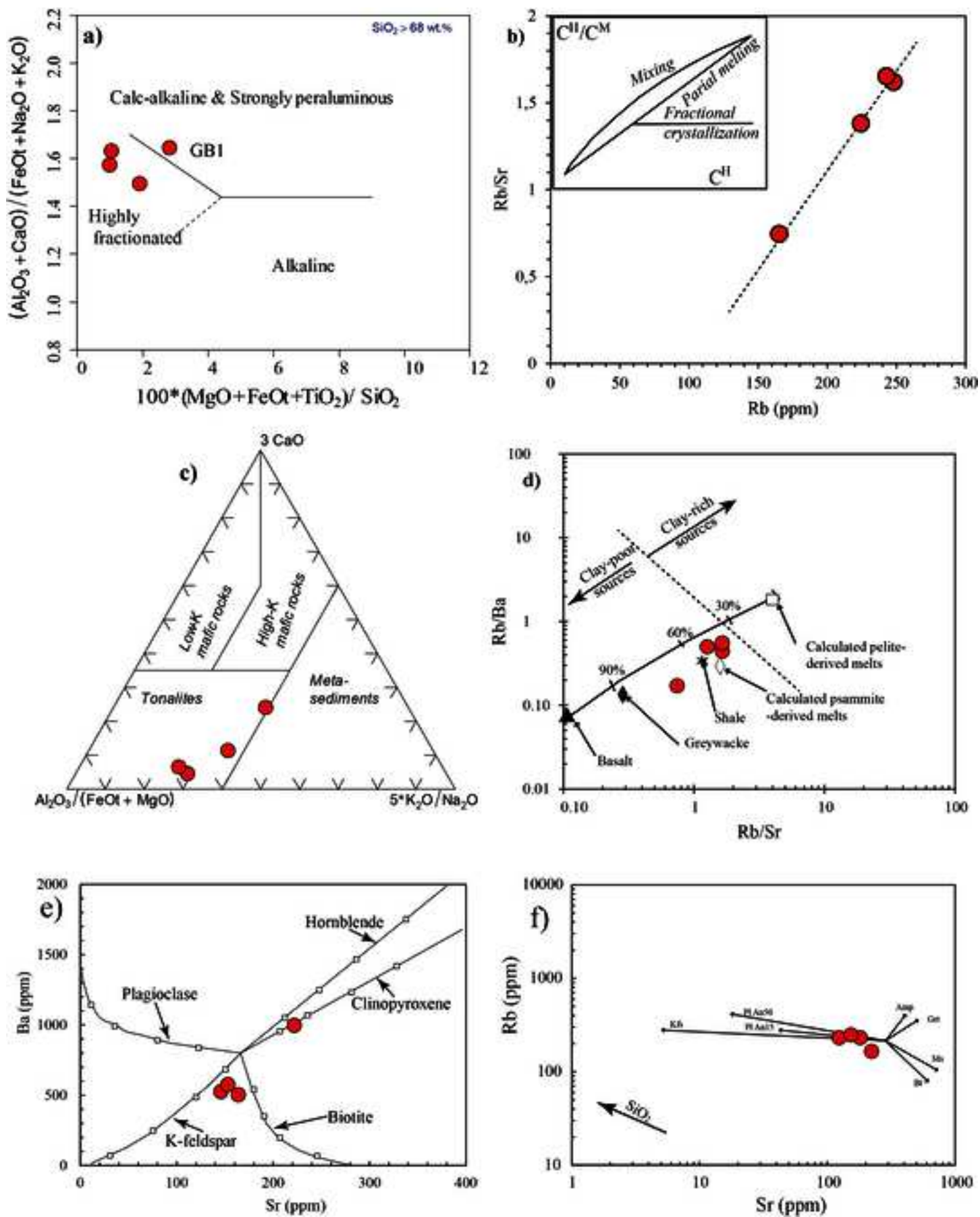


Fig4









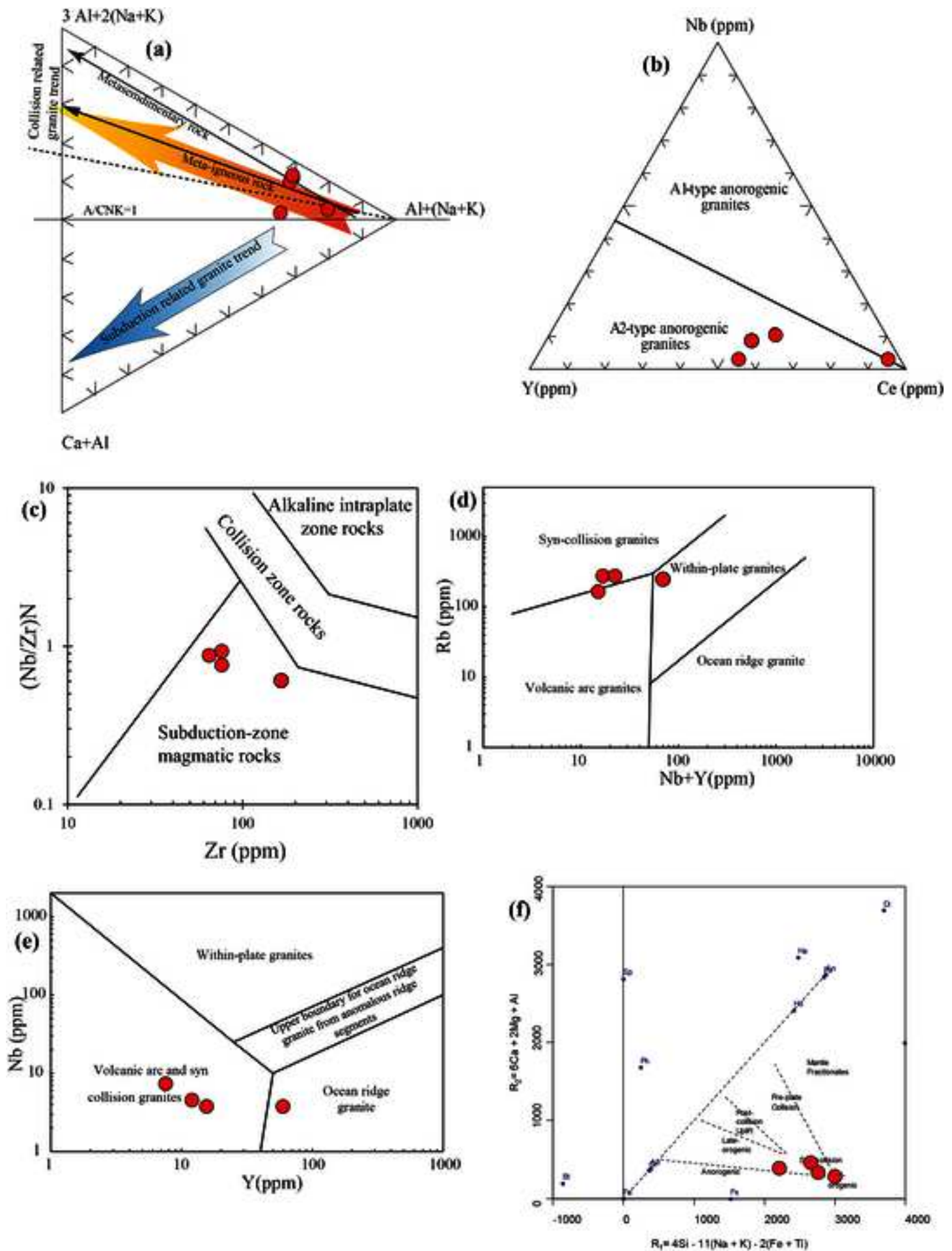


Table 1. LA-ICP-MS U-Th-Pb results for zircons of the Gari-Gombo granite.

Sample	$f_{206C}\%$	U(ppm)	Th/U	Pb(ppm)	$^{207}Pb/^{235}U$	2se%	$^{206}Pb/^{238}U$	2se%	Rho	$^{207}Pb/^{206}Pb$	2se (abs)	$^{206}Pb/^{238}U$	2se (abs)	$^{207}Pb/^{235}U$	2se (abs)	% conc
GB1-01.d	11.66	1611	0.05	2135	2.2482	5.7	0.10342	3.7	0.04	2415	81	634	22	1196	40	53.0
GB1-02.d	3.30	310	0.28	498	1.9274	5.8	0.14598	3.8	-0.01	1540	90	878	31	1091	39	80.5
GB1-03.d	15.49	2211	0.26	4436	2.9401	5.2	0.11143	3.7	0.47	2743	68	681	24	1392	40	48.9
GB1-04.d	3.58	184	0.26	185	1.2831	5.9	0.10331	3.8	0.34	1427	94	634	23	838	34	75.6
GB1-05.d	3.46	3461	0.09	1674	1.2395	5.2	0.10152	3.7	0.48	1400	78	623	22	819	29	76.1
GB1-06.d	3.65	388	0.72	726	1.2432	5.4	0.10055	3.9	0.32	1430	85	618	23	820	30	75.3
GB1-07.d	0.32	372	0.54	561	0.8732	5.7	0.10039	4.1	0.40	708	101	617	24	637	27	96.8
GB1-8.d	1.47	359	0.55	552	1.0117	5.6	0.10030	3.8	0.15	996	95	616	23	710	28	86.8
GB1-9.d	4.15	3777	0.08	2262	1.3298	5.4	0.10101	3.7	0.35	1515	82	620	22	859	31	72.2
GB1-10.d	0.00	772	0.54	1701	2.7589	5.3	0.17497	3.8	0.38	1848	77	1039	36	1344	39	72.8
GB1-11.d	20.55	2248	0.15	6436	3.5810	5.2	0.11075	3.9	0.66	3055	66	677	25	1545	42	43.8
GB1-12.d	0.00	470	0.89	2778	6.2597	5.2	0.17033	3.7	0.47	3281	64	1014	34	2013	45	61.3
GB1-13.d	0.02	2609	0.02	150	0.8314	5.2	0.09914	3.7	0.60	615	88	609	22	614	24	99.2
GB1-14.d	7.81	435	0.65	748	1.7912	5.5	0.10350	3.7	0.34	2024	79	635	23	1042	36	60.9
GB1-15.d	2.00	3371	0.09	1680	1.0652	5.7	0.10063	3.7	0.25	1115	95	618	22	736	30	83.9
GB1-16.d	15.68	203	1.11	642	2.8150	5.3	0.10433	3.7	0.35	2797	70	640	23	1360	40	47.1
GB1-17.d	5.55	2157	0.05	1561	1.4845	5.2	0.10195	3.7	0.62	1731	75	626	22	924	32	67.7
GB1-18.d	3.01	2463	0.26	3293	1.8509	5.6	0.14486	3.8	0.36	1489	86	872	31	1064	37	82.0
GB1-19.d	0.00	1755	0.02	118	0.8447	5.2	0.10071	3.7	0.41	613	89	619	22	622	24	99.5
GB1-20.d	4.41	420	0.86	613	1.5459	5.3	0.11344	3.7	0.23	1599	79	693	24	949	33	73.0
GB1-21.d	1.26	3383	0.04	855	0.9799	5.2	0.10019	3.7	0.52	946	83	616	21	694	26	88.7
GB1-22.d	0.00	462	0.45	1581	5.8498	5.4	0.24647	3.8	0.68	2573	70	1420	49	1954	46	75.9
GB1-23.d	2.04	2102	0.23	1745	1.0843	5.2	0.10195	3.7	0.43	1128	82	626	22	746	27	83.9
GB1-24.d	3.36	504	0.28	509	1.2753	5.8	0.10456	4.0	0.48	1394	89	641	24	835	33	76.8
GB1-25.d	2.62	3767	0.04	1244	1.1279	5.4	0.10071	4.0	0.42	1242	84	619	24	767	29	80.7
GB1-26.d	0.00	6663	0.17	4467	0.8427	5.1	0.10116	3.6	0.66	610	86	621	22	621	24	100.1
GB1-27.d	3.50	2125	0.02	767	1.2415	7.2	0.10185	3.8	0.55	1409	117	625	23	820	41	76.3
GB1-28.d	0.99	247	0.38	283	0.9611	6.0	0.10215	4.0	0.27	891	105	627	24	684	30	91.7

GB1-29.d	2.27	3147	0.17	1166	1.0967	5.4	0.10096	3.9	0.59	1173	84	620	23	752	29	82.5
GB1-30.d	1.54	554	0.62	831	1.0168	5.4	0.10111	3.7	0.34	1017	87	621	22	712	27	87.2
GB1-31.d	2.38	2430	0.08	1077	1.1283	5.6	0.10195	4.0	0.84	1199	82	626	24	767	30	81.6
GB1-32.d	0.37	438	0.40	470	0.9040	5.4	0.10327	3.8	0.38	737	92	634	23	654	26	96.9
GB1-33.d	2.64	3777	0.05	1511	1.1360	5.6	0.10072	3.8	0.39	1245	89	619	22	771	30	80.3
GB1-34.d	3.34	1157	0.28	1168	1.2480	5.3	0.10295	3.8	0.40	1384	81	632	23	823	30	76.8
GB1-35.d	2.10	4280	0.04	1388	1.0830	5.2	0.10109	3.7	0.48	1138	82	621	22	745	28	83.3
GB1-36.d	0.00	443	0.60	731	0.8432	5.2	0.10153	3.7	0.31	616	90	623	22	621	24	100.4
GB1-37.d	10.27	2797	0.12	3130	2.0344	5.8	0.10302	4.1	0.53	2285	80	632	24	1127	39	56.1
GB1-38.d	1.35	1789	0.18	1048	1.0015	5.4	0.10144	3.7	0.45	973	87	623	22	705	27	88.4
GB1-39.d	10.55	4116	0.09	5684	2.4938	5.8	0.11888	3.8	0.64	2348	79	724	26	1270	42	57.0
GB1-40.d	11.39	390	0.38	1082	3.1591	5.8	0.14309	4.1	0.29	2477	84	862	33	1447	45	59.6
GB1-41.d	3.08	2236	0.12	1193	1.1963	6.0	0.10177	4.1	0.38	1333	97	625	24	799	33	78.2
GB1-42.d	13.38	747	0.56	2273	2.7701	5.2	0.11566	3.7	0.52	2584	68	706	25	1348	39	52.4
GB4-01.d	39.25	11657	0.06	21158	2.7477	5.9	0.05394	4.1	0.82	3786	65	339	14	1341	44	25.2
GB4-02.d	12.66	436	0.21	1034	2.6777	4.7	0.11570	2.2	0.29	2526	71	706	14	1322	35	53.4
GB4-03.d	0.06	1537	0.02	104	0.8620	4.3	0.10208	1.9	0.44	643	81	627	12	631	20	99.3
GB4-04.d	0.00	2504	0.01	74	0.8653	4.3	0.10344	1.9	0.47	611	81	635	12	633	20	100.2
GB4-05.d	0.00	533	0.17	1208	5.0111	4.9	0.25223	3.0	0.54	2272	75	1450	39	1821	41	80.2
GB4-06.d	26.36	1970	0.48	2263	1.6558	4.2	0.04543	1.9	0.64	3267	57	286	5	992	27	28.9
GB4-07.d	0.05	244	0.47	481	1.5672	4.5	0.15956	2.0	0.33	965	82	954	18	957	28	99.7
GB4-8.d	6.21	757	0.04	514	1.4622	4.6	0.09637	2.4	0.44	1805	75	593	14	915	28	64.8
GB4-9.d	2.31	3394	0.02	813	1.0946	4.9	0.10032	2.1	0.21	1178	88	616	12	751	26	82.1
GB4-10.d	3.60	6772	0.08	3609	1.1746	4.7	0.09511	2.3	0.73	1402	74	586	13	789	26	74.3
GB4-11.d	8.00	3892	0.03	2577	1.4836	4.4	0.08685	1.9	0.45	2003	67	537	10	924	27	58.1
GB4-12.d	0.58	2404	0.19	1886	1.2289	4.4	0.12753	2.2	0.68	922	77	774	16	814	25	95.1
GB4-13.d	0.14	2657	0.01	101	0.8561	4.4	0.10084	2.2	0.60	660	81	619	13	628	20	98.6
GB4-14.d	0.10	162	0.44	195	0.8632	5.4	0.10231	2.4	0.05	658	112	628	14	632	25	99.4
GB4-15.d	0.04	4046	0.01	207	0.8878	4.6	0.10455	2.6	0.85	652	80	641	16	645	22	99.4
GB4-16.d	1.69	235	0.25	290	1.5178	4.6	0.13678	2.0	0.24	1211	81	826	16	938	28	88.1

GB4-17.d	0.00	5613	0.00	83	0.8484	4.2	0.10173	1.8	0.71	603	78	625	11	624	20	100.1
GB4-18.d	3.41	400	0.40	746	1.4570	4.3	0.11645	1.9	0.29	1448	73	710	13	913	26	77.8
GB4-19.d	6.71	4702	0.03	1707	1.2056	4.6	0.07828	2.1	0.62	1820	71	486	10	803	26	60.5
GB4-20.d	16.22	3837	0.01	5570	2.7510	5.3	0.10300	2.4	0.39	2771	76	632	15	1342	39	47.1
GB4-21.d	1.49	636	0.86	2150	1.5923	4.5	0.14357	2.1	0.25	1202	82	865	17	967	28	89.4
GB4-22.d	0.00	936	0.03	507	5.7989	4.4	0.27316	2.0	0.73	2380	63	1557	28	1946	38	81.8
GB4-23.d	2.51	326	0.18	343	1.7147	4.4	0.14056	1.9	0.36	1384	74	848	15	1014	28	83.6
GB4-24.d	2.51	206	0.30	226	1.6333	4.7	0.13613	1.9	0.24	1367	80	823	15	983	29	83.7
GB4-25.d	0.05	215	0.41	238	0.8924	4.8	0.10585	2.3	0.23	663	93	649	14	648	23	100.1
GB4-26.d	0.00	161	0.68	1079	13.6731	4.4	0.48632	2.0	0.74	2860	60	2555	42	2727	41	95.4
GB4-27.d	2.42	8474	0.01	1161	0.6693	4.6	0.06552	1.9	0.14	1055	84	409	7	520	19	78.6
GB4-28.d	0.19	208	0.50	420	1.5093	4.6	0.15472	2.2	0.16	973	86	927	19	934	28	99.3
GB4-29.d	2.05	2979	0.03	549	0.8228	4.3	0.08087	1.9	0.73	1038	74	501	9	610	20	82.2
GB4-30.d	3.68	945	0.34	1439	1.6517	4.5	0.12636	2.0	0.32	1530	75	767	14	990	28	77.5
GB4-31.d	1.10	3121	0.01	440	0.9647	4.2	0.10071	1.8	0.47	910	75	619	10	686	21	90.2
GB4-32.d	0.27	3667	0.03	462	0.8807	4.6	0.10218	2.8	0.60	704	86	627	17	641	22	97.8
GB4-33.d	0.00	222	0.09	90	1.5086	4.5	0.15807	2.0	0.47	905	80	946	17	934	27	101.3
GB4-34.d	1.85	2148	0.07	1238	1.5473	4.5	0.13704	2.3	0.65	1245	75	828	18	949	28	87.2
GB4-35.d	4.99	781	0.18	965	1.6376	4.4	0.11415	1.8	0.41	1690	70	697	12	985	27	70.8
GB4-36.d	0.79	3870	0.01	391	0.9525	4.2	0.10254	1.8	0.55	842	76	629	11	679	21	92.6
GB4-37.d	0.00	432	0.36	738	1.7717	4.4	0.16979	2.0	0.49	1092	76	1011	19	1035	28	94.8
GB4-38.d	1.69	7396	0.01	1065	0.9407	4.5	0.09314	2.0	0.38	1014	77	574	11	673	22	85.3
GB4-39.d	1.10	2285	0.25	2647	1.5083	4.4	0.14245	2.0	0.48	1115	77	858	16	934	27	91.9
GB4-40.d	0.02	2894	0.00	58	0.8614	4.4	0.10224	1.9	0.58	634	80	628	12	631	21	99.5
GB4-41.d	3.88	183	0.22	171	1.1343	4.7	0.09060	2.1	0.28	1434	80	559	11	770	26	72.6
GB4-42.d	1.07	2350	0.15	921	0.8896	4.4	0.09444	1.8	0.54	871	79	582	10	646	21	90.0

$$f_{206} \% = \frac{(^{207}\text{Pb}/^{206}\text{Pb})_{\text{m}} - (^{207}\text{Pb}/^{206}\text{Pb})_{\text{*}}}{(^{207}\text{Pb}/^{206}\text{Pb})_{\text{c}} - (^{207}\text{Pb}/^{206}\text{Pb})_{\text{*}}} \times 100.$$

if Age $^{206}\text{Pb}/^{238}\text{U} < 1000\text{Ma}$ concordance % = $(\text{Age } ^{206}\text{Pb}/^{238}\text{U} / \text{Age } ^{207}\text{Pb}/^{235}\text{U}) * 100$; else concordance % = $(\text{Age } ^{207}\text{Pb}/^{235}\text{U} / \text{Age } ^{207}\text{Pb}/^{206}\text{Pb})$

* 100. Bold analyses are used for concordia age

Table 2. Selected electron microprobe analyses of monazite from granite (sample GB4) of Gari-Gombo area

Sample	No.	P2O5	La2O3	Ce2O3	Pr2O3	Nd2O3	Sm2O3	Gd2O3	Y2O3	SiO2	CaO	ThO2	UO2	PbO	Total	XGdPO4	XYPO4	ThSuz	ThO2*	age (Ma)	2 σ (Ma)
GB4-M1-1	6	26.06	14.01	27.42	2.74	10.19	1.46	0.81	0.71	2.56	0.75	11.82	0.357	0.343	99.23	0.011	0.015	11.434	13.007	620 \pm	16
GB4-M1-2	7	25.54	12.41	25.42	2.61	10.27	1.79	1.21	1.35	2.82	0.84	13.74	0.510	0.420	98.91	0.016	0.029	13.571	15.437	639 \pm	13
GB4-M1-3	8	25.25	13.37	26.18	2.65	9.99	1.44	0.79	0.64	3.02	0.77	13.87	0.407	0.410	98.78	0.011	0.014	13.380	15.221	632 \pm	13
GB4-M1-4	9	25.86	13.26	26.35	2.78	10.49	1.67	1.05	0.95	2.66	0.71	12.60	0.529	0.388	99.30	0.014	0.021	12.624	14.360	634 \pm	14
GB4-M1-5	10	28.25	13.68	26.87	2.76	10.34	1.87	1.43	1.94	1.44	1.02	8.92	0.420	0.262	99.20	0.019	0.041	9.065	10.311	597 \pm	20
GB4-M1-6	11	28.50	13.56	26.90	2.80	10.44	1.85	1.38	2.19	1.21	1.08	8.34	0.473	0.250	98.97	0.018	0.046	8.714	9.911	593 \pm	20
GB4-M1-7	12	27.89	13.52	26.99	2.80	10.45	1.87	1.40	1.73	1.53	0.99	9.20	0.434	0.273	99.07	0.019	0.037	9.359	10.645	603 \pm	19
GB4-M1-8	13	27.12	14.13	29.02	3.04	11.65	2.27	1.56	0.88	1.77	0.26	7.13	0.084	0.181	99.09	0.021	0.019	6.508	7.405	573 \pm	27
GB4-M1-9	14	29.64	13.64	27.22	2.88	11.20	2.24	1.79	2.01	0.51	1.34	5.77	0.506	0.183	98.92	0.023	0.042	6.547	7.444	578 \pm	27
GB4-M1-10	15	29.06	13.57	27.80	2.95	11.56	2.26	1.61	1.60	0.83	1.00	6.63	0.484	0.217	99.57	0.021	0.034	7.246	8.240	618 \pm	25
GB4-M1-11	16	27.79	13.40	26.54	2.83	11.02	2.13	1.56	1.98	1.61	1.12	7.61	0.434	0.206	98.23	0.021	0.042	7.952	9.044	536 \pm	22
GB4-M1-12	17	25.35	12.46	24.29	2.63	9.86	1.68	1.36	2.01	2.68	1.11	13.40	0.506	0.378	97.72	0.018	0.044	13.252	15.074	589 \pm	13
GB4-M1-13	18	28.40	13.95	28.12	2.93	11.59	2.27	1.66	1.04	1.04	0.81	6.86	0.214	0.184	99.07	0.022	0.022	6.654	7.569	570 \pm	27
GB4-M1-19	24	28.99	13.40	26.56	2.71	10.18	1.83	1.39	2.41	1.01	1.36	8.22	0.523	0.261	98.83	0.018	0.051	8.758	9.961	615 \pm	20
GB4-M3-1	26	28.17	12.61	26.13	2.86	10.85	2.19	1.71	2.10	1.41	1.11	9.21	0.464	0.288	99.07	0.023	0.045	9.451	10.750	628 \pm	19
GB4-M3-2	27	28.60	13.16	26.09	2.72	10.17	1.85	1.53	2.51	1.22	1.22	8.88	0.532	0.280	98.77	0.020	0.053	9.364	10.650	618 \pm	19
GB4-M3-3	28	26.63	12.62	25.63	2.73	10.34	1.93	1.34	1.62	2.38	0.79	12.21	0.519	0.373	99.11	0.018	0.035	12.249	13.933	628 \pm	15
GB4-M3-4	29	26.58	13.31	26.74	2.76	10.51	1.80	1.12	1.14	2.36	0.81	11.00	0.645	0.333	99.09	0.015	0.025	11.552	13.139	596 \pm	15
GB4-M3-5	30	25.97	12.22	24.54	2.61	9.88	1.76	1.44	2.40	2.79	0.83	13.28	0.521	0.400	98.63	0.020	0.052	13.197	15.012	625 \pm	13
GB4-M3-6	31	28.33	12.35	25.98	2.81	10.97	2.18	1.76	2.15	1.40	1.13	9.29	0.495	0.286	99.13	0.023	0.046	9.617	10.938	614 \pm	18
GB4-M3-7	32	28.01	13.30	26.91	2.80	10.72	1.94	1.45	1.70	1.59	0.98	9.53	0.468	0.300	99.72	0.019	0.036	9.749	11.089	634 \pm	18
GB4-M3-8	33	29.05	13.51	26.66	2.69	10.21	1.77	1.45	2.36	0.98	1.22	8.07	0.540	0.265	98.77	0.019	0.050	8.674	9.865	631 \pm	21
GB4-M3-9	34	26.40	12.59	25.20	2.69	9.92	1.73	1.34	2.19	2.55	0.74	12.67	0.484	0.385	98.89	0.018	0.048	12.554	14.280	633 \pm	14
GB4-M3-10	35	25.21	13.32	26.44	2.68	10.10	1.47	0.81	0.80	3.08	0.78	13.17	0.388	0.374	98.62	0.011	0.018	12.707	14.456	607 \pm	14
GB4-M3-11	36	28.90	13.37	26.32	2.72	10.15	1.83	1.52	2.54	1.08	1.39	8.34	0.549	0.260	98.96	0.020	0.054	8.938	10.165	601 \pm	20
GB4-M3-12	37	26.97	13.53	26.50	2.72	10.29	1.61	1.13	1.45	2.46	0.92	11.06	0.473	0.328	99.44	0.015	0.031	11.105	12.632	609 \pm	16
GB4-M3-13	38	26.57	12.31	25.38	2.72	10.44	1.92	1.43	1.76	2.35	0.94	12.29	0.507	0.359	98.98	0.019	0.038	12.286	13.975	603 \pm	14
GB4-M3-14	39	25.62	12.97	25.84	2.71	10.25	1.71	1.10	1.25	2.63	0.93	12.63	0.733	0.376	98.75	0.015	0.027	13.238	15.057	586 \pm	13
GB4-M3-15	40	26.97	13.30	26.91	2.79	10.82	1.85	1.21	1.18	2.17	0.73	10.70	0.683	0.339	99.67	0.016	0.025	11.410	12.977	614 \pm	16

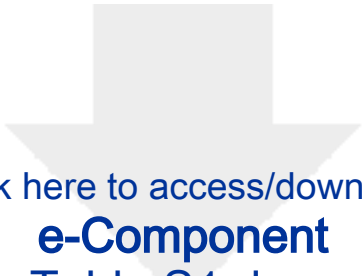
GB4-M3-16	41	26.51	11.89	24.83	2.71	10.21	1.99	1.55	2.22	2.36	0.93	12.42	0.535	0.366	98.54	0.021	0.048	12.485	14.201	605 ±	14
GB4-M3-17	42	25.52	13.55	26.32	2.66	10.20	1.62	1.00	0.99	2.72	0.70	12.82	0.369	0.377	98.83	0.014	0.022	12.351	14.051	629 ±	14
GB4-M3-18	43	25.53	13.51	26.61	2.72	10.23	1.55	0.91	0.79	2.75	0.64	12.95	0.404	0.375	98.97	0.012	0.017	12.564	14.293	616 ±	14
GB4-M2-1	44	28.64	13.29	28.00	3.03	11.61	2.63	1.81	1.51	1.15	0.71	5.90	0.346	0.172	98.80	0.024	0.032	6.200	7.051	575 ±	29
GB4-M2-2	45	26.67	12.86	26.49	2.83	10.91	2.37	1.62	1.43	2.35	1.10	7.20	0.310	0.173	96.30	0.022	0.031	7.227	8.220	495 ±	25
GB4-M2-3	46	27.93	13.55	27.41	2.96	11.23	2.23	1.46	1.30	1.45	0.77	8.04	0.222	0.221	98.76	0.020	0.028	7.713	8.775	590 ±	23
GB4-M2-4	47	27.19	13.26	26.71	2.83	10.66	1.80	1.32	1.47	1.91	0.93	9.89	0.363	0.289	98.62	0.018	0.032	9.754	11.096	611 ±	18
GB4-M2-5	48	27.17	14.24	28.27	2.97	11.36	2.06	1.37	1.51	1.55	1.23	4.14	0.036	0.086	96.00	0.018	0.032	3.744	4.260	477 ±	48
GB4-M2-9	52	28.99	13.52	26.61	2.75	10.20	1.83	1.46	2.38	1.06	1.28	8.17	0.524	0.266	99.04	0.019	0.050	8.722	9.919	630 ±	20
GB4-M2-10	53	27.45	13.15	26.54	2.76	10.53	1.89	1.39	1.53	1.67	1.05	10.08	0.417	0.297	98.76	0.018	0.033	10.083	11.469	609 ±	18
GB4-M2-11	54	28.54	13.08	26.74	2.82	10.71	2.10	1.56	1.93	1.35	1.10	8.24	0.691	0.273	99.13	0.021	0.041	9.269	10.540	609 ±	19
GB4-M2-12	55	27.25	13.26	25.90	2.92	11.13	2.35	1.67	2.42	1.73	0.87	6.84	0.451	0.197	97.00	0.022	0.052	7.329	8.335	556 ±	24
GB4-M2-14	57	28.59	14.41	27.91	2.76	10.39	1.73	1.31	1.66	1.21	0.96	7.69	0.375	0.234	99.22	0.017	0.035	7.859	8.939	614 ±	23
GB4-M2-15	58	27.67	12.61	26.01	2.80	10.46	2.13	1.67	2.13	1.56	1.20	8.42	0.500	0.260	97.41	0.022	0.046	8.865	10.083	606 ±	20
GB4-M2-16	59	27.15	13.83	27.80	2.89	11.10	2.01	1.23	1.15	1.98	0.83	8.24	0.355	0.224	98.78	0.016	0.025	8.275	9.413	560 ±	22
GB4-M4-1	61	26.16	12.23	24.62	2.60	9.85	1.75	1.40	2.36	2.76	0.80	13.28	0.512	0.404	98.70	0.019	0.051	13.174	14.985	633 ±	13
GB4-M4-2	62	26.49	12.69	25.34	2.62	9.86	1.70	1.29	2.31	2.49	0.78	12.55	0.489	0.386	98.99	0.017	0.050	12.462	14.176	639 ±	14
GB4-M4-3	63	24.43	12.80	24.91	2.50	9.24	1.45	0.93	1.17	3.37	0.89	15.13	0.334	0.380	97.53	0.013	0.026	14.269	16.233	550 ±	12
GB4-M4-4	64	26.36	12.95	25.64	2.67	9.81	1.65	1.27	2.18	2.40	0.87	11.90	0.419	0.374	98.49	0.017	0.047	11.693	13.301	659 ±	15
GB4-M4-5	65	26.05	12.44	25.54	2.77	10.55	1.89	1.28	1.46	2.44	0.85	12.37	0.495	0.372	98.52	0.017	0.032	12.327	14.021	622 ±	14
GB4-M4-6	66	28.19	14.55	28.39	2.88	10.68	1.70	1.12	1.33	1.28	0.87	7.60	0.208	0.210	99.01	0.015	0.028	7.288	8.292	596 ±	24
GB4-M4-7	67	28.10	15.33	30.16	3.02	11.66	1.99	1.24	0.86	1.24	0.24	5.42	0.050	0.147	99.46	0.016	0.018	4.910	5.587	616 ±	36
GB4-M4-8	68	26.55	12.74	25.41	2.67	10.04	1.75	1.33	2.31	2.30	0.78	11.87	0.377	0.370	98.50	0.018	0.050	11.540	13.128	661 ±	15
GB4-M6-2	71	28.02	15.19	29.33	3.02	11.43	2.01	1.41	1.28	1.26	0.48	4.51	0.129	0.112	98.19	0.019	0.027	4.343	4.941	531 ±	41
GB4-M6-3	72	25.83	14.85	28.45	2.91	11.22	2.12	1.33	1.13	2.59	1.16	3.84	0.047	0.092	95.56	0.018	0.024	3.510	3.993	543 ±	51
GB4-M6-4	73	28.77	14.50	29.01	3.00	11.78	2.24	1.54	0.86	0.88	0.71	5.40	0.079	0.141	98.90	0.020	0.018	4.978	5.664	583 ±	36
GB4-M6-6	75	28.41	15.58	28.79	2.99	11.93	2.31	1.45	0.79	0.95	1.16	2.83	0.030	0.076	97.28	0.019	0.017	2.571	2.925	610 ±	69
GB4-M8-1	76	23.89	12.53	24.14	2.46	9.06	1.34	0.96	1.31	3.31	1.26	15.32	0.400	0.437	96.42	0.013	0.029	14.635	16.649	617 ±	12
GB4-M8-2	77	26.90	13.32	26.82	2.81	10.69	1.98	1.39	1.44	1.93	0.74	9.52	0.430	0.285	98.26	0.019	0.031	9.626	10.949	611 ±	18
GB4-M8-3	78	27.08	14.46	28.05	2.83	10.63	1.76	1.11	0.96	1.83	0.68	8.94	0.328	0.254	98.91	0.015	0.021	8.813	10.026	595 ±	20
GB4-M9-1	80	27.54	14.07	27.80	2.82	10.81	1.95	1.37	1.51	1.73	0.78	7.91	0.387	0.231	98.91	0.018	0.032	8.087	9.199	591 ±	22
GB4-M5-1	84	29.71	13.55	27.14	2.79	10.58	2.05	1.61	2.07	0.64	1.34	6.92	0.635	0.235	99.28	0.021	0.044	7.943	9.032	610 ±	22
GB4-M5-2	85	30.09	13.91	27.21	2.89	11.31	2.37	1.97	2.09	0.28	1.18	4.24	1.114	0.202	98.85	0.026	0.044	6.988	7.941	597 ±	26
GB4-M5-3	86	28.56	14.97	29.62	3.10	11.97	2.15	1.37	1.00	0.94	0.50	4.01	0.407	0.129	98.73	0.018	0.021	4.713	5.359	566 ±	38

GB4-M5-4	87	29.82	14.07	27.90	2.91	11.33	2.51	1.95	1.97	0.26	0.96	3.17	1.225	0.177	98.25	0.026	0.042	6.361	7.226	577 ±	28
GB4-M5-8	91	28.25	13.68	27.17	2.75	10.61	1.84	1.44	1.89	1.28	0.99	8.29	0.429	0.252	98.85	0.019	0.040	8.538	9.711	608 ±	21
GB4-Msm1	92	24.31	9.85	17.80	2.16	8.05	1.79	2.29	14.60	2.34	1.01	5.17	0.335	0.135	89.82	0.030	0.307	5.514	6.271	507 ±	32
GB4-M7-1	93	27.83	13.43	26.52	2.71	10.32	1.74	1.25	1.81	1.64	0.99	9.95	0.506	0.305	99.01	0.017	0.039	10.226	11.631	616 ±	17
GB4-M7-2	94	24.61	12.88	25.45	2.64	9.93	1.47	0.87	0.66	3.44	0.60	15.92	0.480	0.469	99.40	0.012	0.014	15.404	17.523	628 ±	12
GB4-M7-3	95	28.75	13.46	26.82	2.72	10.51	1.90	1.44	2.04	1.29	1.03	8.64	0.469	0.265	99.33	0.019	0.043	8.963	10.194	610 ±	20
GB4-M7-4	96	28.34	13.03	26.83	2.82	10.81	1.98	1.49	1.81	1.48	0.98	8.96	0.451	0.270	99.25	0.020	0.039	9.198	10.462	606 ±	19
GB4-M7-5	97	28.33	13.05	26.68	2.77	10.70	2.05	1.55	1.86	1.42	1.02	8.91	0.445	0.270	99.04	0.021	0.040	9.135	10.391	609 ±	19
Madmon20	mean	25.31	8.17	25.18	3.64	14.98	4.26	1.92	0.93	3.01	0.13	11.27	0.420	0.272	99.49	0.026	0.020	11.126	12.657	507 ±	16


Table 3. Major oxides and trace element analyses of Gari-Gombo granites.

Sample	GB1	GB4	GB5	GB6
Major oxides (wt.%)				
SiO ₂	74.53	78.80	77.61	70.16
TiO ₂	0.23	0.06	0.05	0.12
Al ₂ O ₃	13.76	12.97	13.77	13.60
Fe ₂ O ₃	1.43	0.67	0.65	1.00
MnO	0.02	0.01	0.01	0.02
MgO	0.56	0.20	0.16	0.27
CaO	1.64	0.49	0.45	0.89
Na ₂ O	3.09	3.39	3.30	3.37
K ₂ O	4.97	4.39	5.14	5.38
P ₂ O ₅	0.00	0.03	0.00	0.01
LOI	0.36	0.32	0.31	0.33
Total	100.60	101.33	101.45	95.15
Mg#	43.91	37.33	32.78	34.69
FeOt	1.28	0.6	0.58	0.9
A/CNK	1.02	1.16	1.17	1.05
A/NK	1.32	1.26	1.25	1.20
Trace elements (ppm)				
Rb	165.27	224.34	248.00	242.79
Ba	1003.21	493.66	560.97	520.53
Sr	221.92	162.45	153.09	146.95
Pb	60.47	46.69	43.93	42.46
Th	52.97	18.73	5.86	7.00
U	3.92	6.52	3.30	2.59
Zr	151.64	77.99	66.29	76.15
Hf	4.48	2.67	2.25	2.57
Y	7.67	58.69	15.46	11.95
Nb	7.36	3.78	3.69	4.41
Sc	6.20	3.61	3.61	4.34
Ni	0.29	0.35	2.48	bld
Co	3.05	1.49	1.80	2.09
V	23.44	8.25	9.63	8.80
Ga	34.62	30.20	17.96	18.08
Zn	17.44	16.52	17.70	21.48
Ge	10.81	13.72	2.02	2.37
La	116.10	125.83	13.33	13.76
Ce	225.11	75.31	23.01	24.25
Pr	24.41	29.30	2.63	2.69
Nd	90.29	111.65	9.84	9.96
Sm	12.13	21.10	2.13	2.10
Eu	1.56	4.51	0.69	0.64
Gd	6.60	17.40	2.42	2.16
Tb	0.50	2.22	0.37	0.32
Dy	1.95	11.64	2.33	1.90
Ho	0.28	1.90	0.45	0.37
Er	0.63	4.85	1.34	1.05
Tm	0.09	0.62	0.20	0.15
Yb	0.54	3.91	1.50	0.97
Lu	0.07	0.51	0.22	0.13

Eu/Eu*	0.53	0.71	0.93	0.91
(La/Yb) _N	148.18	22.27	6.17	9.80



Click here to access/download
e-Component
Table S1.docx



Highlights

- The ca 631– 620 Ma Gari-Gombo pluton emplaced during the D2 regional Pan-African deformation.
- Gari-Gombo pluton intrusive granites represent highly fractionated I-type granite generated by partial melting of partial melting of 2.9 Ga meta-igneous rocks.
- EPMA U-Th-Pb monazite dating of the Gari-Gombo granite yields metamorphic recrystallization ages of $602 \pm \text{Ma}$,

Declaration of interests

The authors declare that they have no known competing financial interests or personal relationships that could have appeared to influence the work reported in this paper.

The authors declare the following financial interests/personal relationships which may be considered as potential competing interests:

Joseph Martial Akame*, Marc Poujol, Vinciane Debaille, Bernhard Schulz, Nathan Cogné, Lise Carole Okomo Atouba, Sébastien Owona

Corresponding author: Joseph Martial AKAME: Laboratoire G-Time, Université libre de Bruxelles, CP 160/02, 50 Avenue F.D. Roosevelt, 1050, Brussels, Belgium.

Email: (akamejosephmartial@gmail.com; joseph.martial.akame@ulb.be)